International Journal of Engineering and Geosciences
https://dergipark.org.tr/en/pub/ijeg
e-ISSN 2548-0960

Accuracy assessment of UAS photogrammetry and structure from motion in surveying and mapping

Sayed Ishaq Deliry [1], **Uğur Avdan** [*2]

[1] *Eskisehir Technical University, Department of Remote Sensing and Geographical Information Systems, Türkiye, deliry.ishaq@gmail.com*
[2] *Eskisehir Technical University, Institute of Earth and Space Sciences, Türkiye, uavdan@eskisehir.edu.tr*

Cite this study: Deliry, S. I., & Avdan, U. (2024). Accuracy assessment of UAS photogrammetry and structure from motion in surveying and mapping. International Journal of Engineering and Geosciences, 9 (2), 165-190

https://doi.org/10.26833/ijeg.1366146

Keywords
Structure from motion
Unmanned aerial systems
Unmanned aerial vehicle
SfM photogrammetry
Rapid surveying

Research Article

Received: 25.09.2023
Revised: 21.11.2023
Accepted: 26.11.2023
Published: 23.07.2024

Abstract

Rapid and accurate surveying has always attracted great interest in all scientific and industrial activities that require high-resolution topographic data. The latest automation and advancement in geomatics engineering are remote sensing solutions using Unmanned Aerial Systems (UAS) and Structure from Motion (SfM) with Multi-View Stereo (MVS) photogrammetry. This research aimed to find the influence of flight height, Ground Control Point (GCP), and software on the geometric accuracy of UAS-SfM-derived Digital Surface Models (DSMs) and orthoimages, as well as to analyze and evaluate the accuracy of UAS-SfM as a rapid and low-cost alternative to conventional survey methods. To achieve the aim of the study, aerial surveys using a fixed-wing UAS and field surveys using RTK GNSS and total station were conducted. A total of 16 photogrammetric projects were processed using different GCP configurations, and detailed statistical analysis was performed on the results. Moreover, the contribution of cross flight on bundle adjustment was investigated empirically by conducting a combined photogrammetric image processing. The analysis revealed that flight height, GCP number and distribution, and the processing software significantly affect products' quality and accuracy. Evaluation of the achieved accuracies was made based on the American Society for Photogrammetry and Remote Sensing (ASPRS) positional accuracy standard for digital geospatial data. The findings of this study revealed that using the optimal flight height and GCP configuration, 3D models, orthomosaics and DSMs can be rapidly reconstructed from 2D images with the quality and accuracy sufficient for most terrain analysis applications, including civil engineering projects.

1. Introduction

Digital elevation models (DEMs) are the primary database for topography-related analysis such as engineering planning, infrastructure design, and earth observations [1, 2]. Very high-resolution 3D models and associated orthoimages derived from Unmanned Aerial Systems (UAS) images are of great importance in scientific fields involving mapping subtle topographic variations and surface analysis, for instance, in structural monitoring and studies of earth surface dynamics [3–5]. Unmanned aerial systems, also known as drones, commonly termed as Unmanned Aerial Vehicles (UAVs), are aircraft systems that operate without a pilot on board. With the development of technology, the application of UAS as a remote sensing platform and SfM-MVS as a photogrammetric and computer vision technique to produce high-resolution topographic maps is increasing [3, 6, 7]. The application of UAS and SfM-MVS is gaining increasing interest in most disciplines, particularly in engineering and earth sciences [5–10]. Photogrammetric applications of UAS are pervasive and in high demand in engineering and geosciences. Recently, UAS-based photogrammetry, commonly known as UAV photogrammetry, is widely used in surveying and 3D modeling applications.

Surveying is a rapidly developing engineering field that has changed dramatically over the past decades and benefited from a wide range of technological advances such as ground-based, water-based, airborne, and spaceborne [11–21]. Engineering surveying includes planning, designing, and conducting surveys of different accuracy classes for development, designing, construction, quality control, inspection, and operation and maintenance of civil and other engineering projects [21–23]. Surveying has a wide engineering professional practice, which provides high-accuracy topographic maps as one of the main activities. Technological

advances related to surveying and mapping have been rapid over the past decades, especially in digital terrain modeling. However, cost and time-consumption are common limitations in conventional methods [11, 24, 25]. In physical surveying using the conventional methods, each individual point is surveyed in a subjective manner in which professional engineering surveyors with sufficient geomorphological knowledge determine where to be measured to get accurate interpolation. The decision on the number and location of points for an accurate representation of topography using traditional methods highly depends on the surveyor's skill. Although highly detailed topographical surveys using physical surveying techniques are possible, these methods are subjective, costly, and extremely time-consuming.

Structure from motion is one of the most recent and important developments in digital surveying [5, 6, 26, 27]. With the advances in computer vision, the combination of digital technology and SfM has revolutionized the photogrammetry field. Motion-based reconstruction was first introduced by Ullman [28] in the late 1970s. SfM became more popular with the development of computer vision algorithms in the 2000s [29–33]. These techniques are used to reconstruct high-quality 3D structures from a range of 2D photogrammetric images. The SfM-MVS algorithms produce true color 3D dense point clouds, which are quite comparable to those of laser scanning surveys. Unlike classic aerial stereophotogrammetry, which requires careful flight planning and camera pre-calibration [34], UAS-based SfM (UAS-SfM) provides simplicity in data acquisition and image processing without the need for comprehensive planning or camera calibration [2]. Today, photogrammetric software packages with high computational power are available that can process hundreds of images simultaneously and extract 3D surface information using feature detection and matching algorithms. With these developments, using a lightweight UAV and a digital non-metric camera, unprecedented high-resolution 3D elevation models can be generated, which are comparable in scale and accuracy to that of terrestrial laser scanner (TLS), airborne laser scanner, and conventional photogrammetric approaches [3, 5]. In addition to achieving more detailed 3D models than traditional photogrammetry methods, SfM-MVS can reduce processing efforts by about 3-6 times [35]. However, in UAS-based surveys, some influential parameters such as the number and distribution of GCPs, flight height, and image overlap can significantly affect the mapping accuracy.

To overcome the limitation of traditional surveying techniques, and to obtain rapid and cost-effective data, the application of UAS-SfM has been the subject of many studies in recent years [10, 11, 36–45]. Very high spatial and temporal resolution images can be provided by combining UAS data and remote sensing techniques. UAVs have distinguished advantages over satellites and human-crewed aircraft, such as higher spatial and temporal resolution, lower cost, availability, rapid data acquisition, and operational flexibility [3, 7, 46–48]. Furthermore, accessibility is a challenging issue in terrestrial surveys where neither TLS nor ground photogrammetry is a practical option. Terrestrial surveys for generating 3D models are quite challenging in many situations, for example, in hazardous areas, steep and narrow valleys, and buildings with slanted roofs. UAS photogrammetry is the solution for such problems; therefore, UAS-SfM can be considered as an effective alternative to traditional photogrammetry.

In engineering works, data accuracy is the most important concern that should be within acceptable limits; hence, accuracy assessment is crucial. Recently, many studies have been conducted to assess the ability of UAS-SfM as an alternative to conventional survey methods. However, each quantitative validation study is different from another due to variations in method, platform, camera, survey scale, terrain, comparison method, and software used for processing. Although many studies have focused on the influence of GCP number and distribution on the accuracy of UAS-SfM products, only a few studies have analyzed the relationship between errors and their distance from the nearest GCP. For example, Ruzgienė et al. [49] examined the accuracy of UAS-SfM-derived DSM; they indicated that the accuracy and quality of DSM mainly depend on sensor resolution, flight height, image overlap, and GCP number and accuracy. The authors reported that by adding 5 more GCPs to a cluster of 5 GCPs, the DSM vertical accuracy improved by 1.5 cm. Long et al. [50] stated that a correlation exists between the number of GCPs and the vertical accuracy; the higher the number of GCPs, the higher the accuracy. Gerke and Przybilla [51] studied direct and indirect georeferencing in the UAS-based survey. As a result of their analysis, the RTK based UAS survey achieved a vertical accuracy of up to 10 cm, while by adding the cross flight data, the accuracy improved to 5 cm, and adding GCPs greatly contributed to the accuracy. Agüera-Vega et al. [11] conducted a study on 60 photogrammetric projects by utilizing a rotary-wing UAS and a non-metric camera. In their analyses, the most accurate results were achieved from 5 to 10 GCPs, which from 50 m flight height, they obtained vertical accuracy of 5 cm. Unlike other studies, Tonkin and Midgley [52] obtained high DSM accuracy using just 4 GCPs. The researchers produced DSMs from UAV images applying a varying number of GCPs (3-101) to study the relation between the number and placement of GCPs. The authors stated that for all DSMs, the vertical error was less than 20 cm. Their results revealed improvements in DSM quality where four and more number of GCPs were used; however, the difference in vertical error between the DSM produced using 4 GCPs (6.4 cm) and the DSM generated by applying 101 GCPs (5.9 cm) was 0.5 cm. The results indicated that the distribution of GCPs is important because vertical error increased as the study points moved away from the GCP cluster. Coveney and Roberts [38] used a fixed-wing UAS with a camera on-board to generate a DEM of an urban area, including a river. The authors investigated the influence of 0 to 61 GCPs in various projects, and as a result, they concluded that using 1 GCP per every 2 ha is sufficient for UAS-based mapping, and no significant

improvements were observed using more than 15 GCPs. Oniga et al. [53] reported that from the images obtained from lower heights (~30 m), using 1 GCP per 200 square meters, 3D data can be produced at the level of 1 to 2 cm. Sanz-Ablanedo et al. [44] analyzed the role of the number and location of GCPs on the geometrical accuracy of DSM. They found that accuracy was greatly improved using 4 GCPs per hundred photos, which made it possible to achieve horizontal accuracy of the same as ground sampling distance (GSD) and vertical accuracy of ±1.5 × GSD. Using fewer GCPs (1 GCP per hundred photos) degraded both horizontal and vertical accuracies to ±4 × GSD and ±5 × GSD, respectively. Martinez-Carricondo et al. [2] evaluated the accuracy of UAS-based mapping by focusing on the variation of GCPs. They concluded that GCPs should be placed at the edge of the study area to achieve optimal planimetric results. However, this configuration did not increase the vertical accuracy. The best results were obtained by stratified and dense distribution of GCPs within the study area, which resulted in horizontal and vertical accuracy of 3.5 and 4.8 cm. In the literature, the GCP and accuracy correlation has not been investigated conclusively; thus, it requires a thorough statistical analysis. Given the sensitivity of the information obtained from UAS-based mapping, and the variation in the accuracy achieved in the literature, in-depth studies are needed to find the influential parameters and evaluate the accuracy of UAS-SfM in surveying applications.

The main objective of this study was to analyze the influence of flight height and GCP distribution on the geometric accuracy of UAS-SfM-derived DSMs and orthoimages, and to evaluates the accuracy of UAS-based surveying by conducting field surveys using a fixed-wing UAS, RTK GNSS, and total station. Analyses were conducted to find the impact of distance from GCPs on planimetric and vertical accuracy. Evaluation of the achieved accuracies was made based on the American Society for Photogrammetry and Remote Sensing (ASPRS) positional accuracy standard for digital geospatial data. In addition, the contribution of cross flight on bundle adjustment was investigated empirically by performing a combined photogrammetric image processing. The research also presents a comparison of the accuracy and performance of three SfM software packages, namely Agisoft PhotoScan, Pix4Dmapper, and 3Dsurvey in the DSM reconstruction from the same sets of UAV images with optimal image processing parameters.

2. Materials and method

2.1. Study area and data acquisition

Eskisehir Technical University Iki Eylul campus was selected as the study area (Figure 1). The campus is located at 39° 48' 57.4" latitude and 30° 31' 55.4" longitude in the Tepebasi district of Eskisehir, Türkiye. The study area covers approximately 35 hectares of the campus, which comprises roads, parking lots, and vegetation. The purpose of adopting the campus as the study area was the presence of vegetated and non-vegetated land cover as well as the ease of obtaining licenses for conducting several close-range flights.

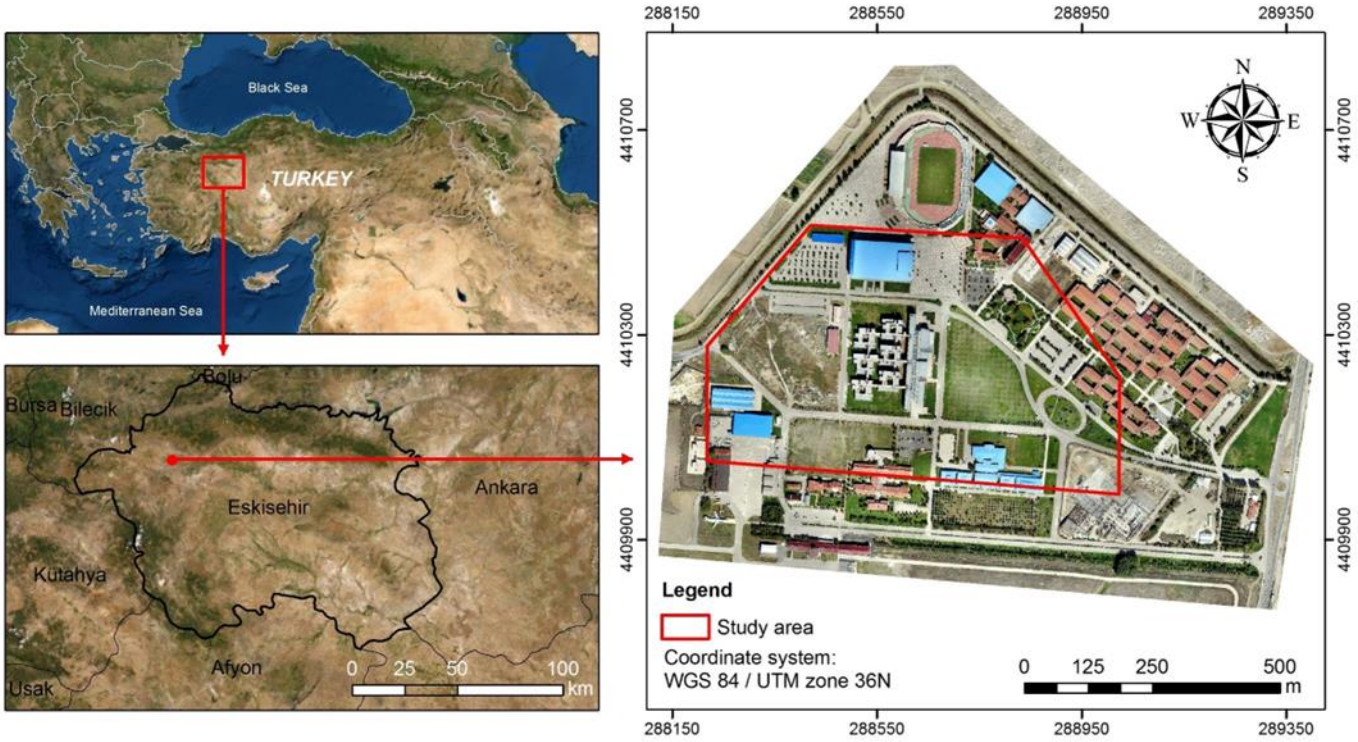

Figure 1. Study area: Eskisehir Technical University Campus.

Project planning is the first and most important step in photogrammetric projects to be carried out extensively. In a particular photogrammetric project, various products can be developed, the final decision on the selection of products, scale, and accuracy is made according to the project requirements. To achieve the

aim of the study, two nadir image acquisition plans were designed to be surveyed using senseFly fixed-wing UAS at average flight heights of 100 and 170 m Above Ground Level (AGL), and 80% and 70%, frontal and 70% and 65% side overlaps to achieve 2.5 and 4.0 cm GSDs, respectively.

According to the new ASPRS standard [54], the GSD of the source imagery should be two times higher or at least equal to the required accuracy. Based on ASPRS Root Mean Square Error (RMSE) accuracy metric, for planimetric works, an accuracy of 1 × GSD is recommended that can be used in the highest accuracy works, 2 × GSD is suitable for standard mapping and GIS tasks, and 3 × GSD and greater is not recommended for measurements, yet can be used for visualization and less accurate estimations. As per ASPRS, the vertical accuracy (non-vegetated) for Class 1 is 1 cm, for Class 2 is 2.5 cm, and for Classes 3 and 4 are 5 and 10 cm, respectively. A fixed-wing UAS covers larger areas by flying at higher altitudes, which considerably reduces the processing time; thus, it is more suitable for surveys of larger areas. Considering this, 2.5 cm and 4 cm GSDs were selected for vertical aerial surveys, which accordingly, the flight altitudes were determined (100 m and 170 m, respectively). Figure 2 illustrates the overall workflow of the methods adopted in this study.

SenseFly eBee Plus fixed-wing UAS was used for photogrammetric image acquisition. The UAS has an onboard GNSS receiver with optional RTK/PPK functionality that is used for navigation and image geotagging. The supplied payload sensor used in this study is a compact 20-megapixel high-resolution SODA RGB camera. The SODA camera is specially developed for UAS photogrammetric works. This camera has a 13.2 x 8.8 mm sensor size, 10.6 mm focal length, and 5472 x 3648-pixel RGB resolution. The area of interest was defined, and flight paths were designed on an aerial map in eMotion 3 flight and data management software. By defining the survey area, ground sampling distance, and image longitudinal and side overlaps, the flight speed was set, and flights were carried out according to the flight path in automatic navigation mode. In the image acquisition process, an operator was responsible for monitoring the take-off and landing, the battery status, the connection between the UAV and ground control system (via a computer stationed at the operating station) for ensuring that the drone is on its designed pathway. Photogrammetric flights at two flight heights were conducted to determine the influence of flight height on the accuracy of products as well as to assess the accuracy of cross flight data in a combined image processing. The photogrammetric characteristics of both flights are shown in the following Table 1.

JAVAD TRIUMPH-1 dual-frequency GNSS receiver was used for the RTK measurements of GCPs and checkpoints. This geodetic instrument has ±1 cm +1 ppm horizontal and ±1.5 cm +1 ppm vertical accuracy, as stated in the manufacturer's specifications. RTK DGNSS technique usually provides high positioning, and the best results can be achieved if the distance to the nearest base station is within 10 km. Since the distance from the study area to the base station is about 9 km, using RTCM (Radio Technical Commission for Maritime Services) and FKP (Flaechen-Korrektur-Parameter) standards, it is possible to achieve vertical and horizontal accuracy within 2 cm. Trimble M3 total station was used for validating GNSS RTK measurement and GCP network adjustment. Trimble M3 has angle measurement accuracy of 2" and 2 mm ±2 ppm distance measurement accuracy. This instrument has the ability of reflectorless measurements of inaccessible points. Figure 3 illustrates the equipment used in this study.

Table 1. Flight and data acquisition parameters

Parameter	Value	
Height above ground level	100 m	170 m
Average flight speed	12.32 m·s^{-1}	11.53 m·s^{-1}
Flight GNSS mode	Standalone	Standalone
Number of strips	13	9
Distance between strips	39 m	66 m
Distance between images (Base)	17 m	51 m
Ground resolution	2.5 cm·px^{-1}	4 cm·px^{-1}
Single image ground coverage	129 x 86 m	219 x 146 m
Number of images	548	155
Forward overlap	80%	70%
Side overlap	70%	65%

GCPs and CPs were marked on the ground and measured accurately using GNSS with differential corrections in real-time kinematic (RTK) mode by connecting to the nearest Continuous Operating Reference Station (CORS). The GCP network was then adjusted using TS measurements. Accurate measurement of the 3D coordinates of GCPs and marking them during the image processing is a time-consuming task, and in challenging terrain, it is difficult to measure a large number of GCPs. According to the literature, in small areas, 5-15 number of GCPs can provide optimum results [11, 55]. Hence, in this study, two GCP clusters (5 and 10) were used to analyze their influence on the accuracy of DSM and orthomosaic. To examine the influence of GCP distribution on the accuracy, and to find the relationship between the vertical accuracy and the distance to the nearest GCP, the positions of 5 GCPs were selected in a way that some checkpoints were outside the GCP polygon. To minimize the distance between the checkpoints and the nearest GCPs, a set of 10 GCPs were formed by adding 5 additional GCPs to the cluster. Figure 4 shows ground control points and checkpoints on vegetated and non-vegetated test areas. GCPs 1-5 were used for the 5 GCP scheme, and for the 10 GCP layout, GCPs from 1-10 were used.

Ground control points are points with known spatial coordinates marked on the ground. These points are measured precisely by terrestrial survey methods such as Differential Global Navigation Satellite System (DGNSS) or total station (TS). GCPs are used for image georeferencing, which includes scale calculation, orientation, and transforming positions to a desired coordinate system [56, 57]. Ground control points can serve as adjustment points or checkpoints (CPs) for accuracy validation of the final product. GCPs are usually marked on a flat surface and evenly distributed within the study area to be visible in at least two images. The number and location of GCPs used to scale a photogrammetric model have a significant impact on the mean error and error distribution within the model [11].

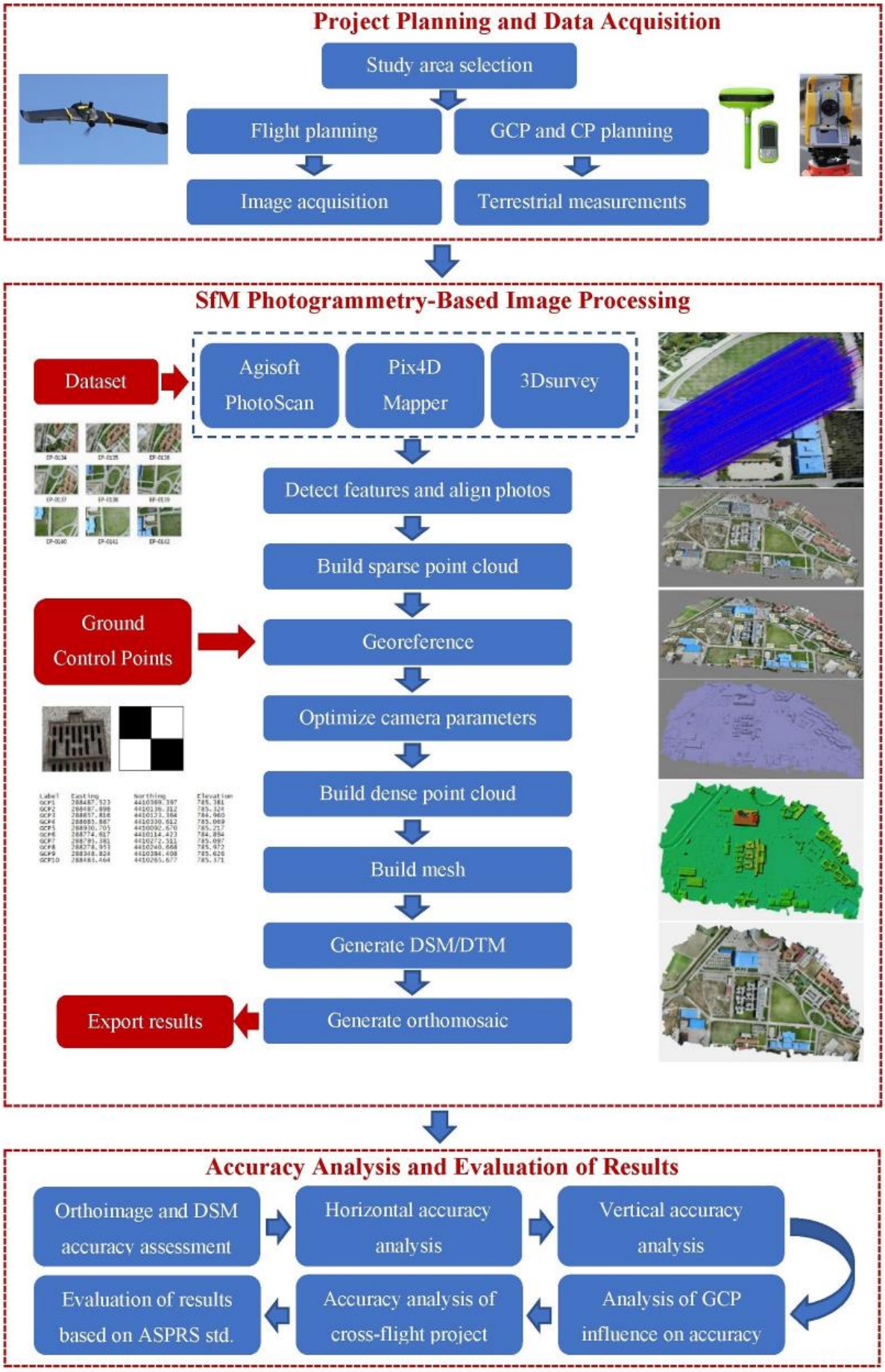

Figure 2. Overall workflow of the methods used in this research. In the SfM image processing section, the left side of the diagram illustrates input data, and the right side shows the generated models, from top to bottom: sparse point cloud, dense point cloud, mesh, DSM, and orthomosaic.

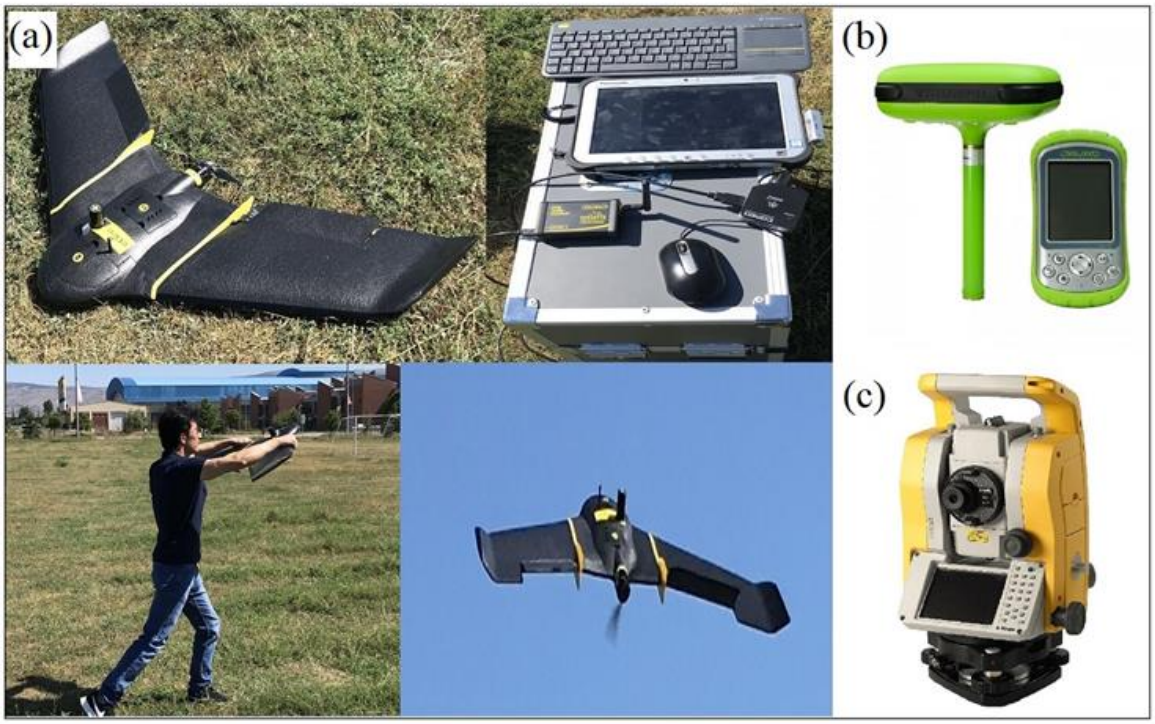

Figure 3. Equipment used in the study: (a) SenseFly eBee Plus with its ground control system used as the photogrammetric platform, and (b and c) GNSS, and TS used as terrestrial measurement instruments, respectively.

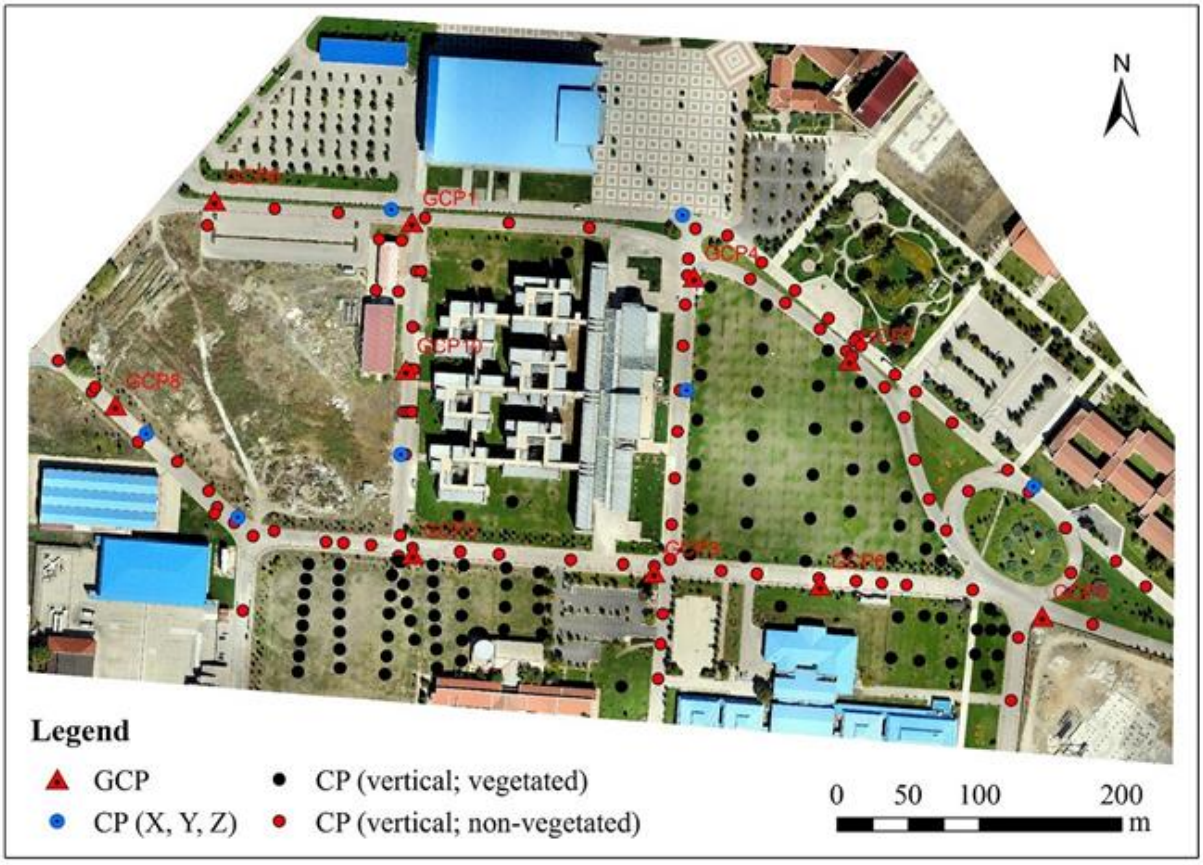

Figure 4. Ground control points and checkpoint.

The number of GCPs depends on the area extent and terrain height difference; the greater the variation, the higher the number of GCPs are required to increase the absolute accuracy [50, 57]. However, using a higher number of GCPs (i.e., more than 10) in small areas does not significantly contribute to higher accuracy; practically, 5 to 10 GCPs are sufficient [51, 52, 57].

Acquired images can be georeferenced directly during the flight or during data processing. If a UAV is equipped with an RTK (Real-Time Kinematic) GPS receiver, this allows images to be directly georeferenced. However, if the data-link connection with the base station is interrupted, the real-time corrections for camera positions will also be affected. The signal interruption will lead to uncertainties that can be improved by using GCPs. Even if the UAV is equipped with a non-RTK ordinary GPS receiver, this will capture georeferenced images with enough metric accuracy to adjust the image bundles and produce maps for emergency response [7]. In the bundle adjustment process based on non-linear least-squares minimization, at least three GCPs are required, which are treated as weighted observations in the least-square minimization [7, 34]. The least-square minimization approach reduces possible deformations and systematic errors of the image block, which leads to the correct estimation of 3D structures [7]. For validating the processing accuracy, checkpoints with known 3D coordinates are used in the process of defining GCPs. When GCPs are defined as CPs, they are not included in the computation of bundle block adjustments, but the software uses these points to find the difference between the interpolated surface coordinates and the actual points to determine the accuracy of the adjustment.

All measurements were performed in Universal Transverse Mercator (UTM) coordinate system, where the World Geodetic System 1984 (WGS 84) reference ellipsoid is the horizontal datum, and as the vertical datum, the Earth Gravitational Model 1996 (EGM96) was selected. A minimum of 6 GPS and 5 GLONASS satellites above 15 degrees in elevation were maintained in all measurements. During the fieldwork, by maintaining a higher number of satellites, PDOP (Position Dilution of Precision) values were in the range of 2.0 to 4.0, indicating the appropriate satellite geometry.

2.2. SfM photogrammetry-based image processing

To generate photogrammetric products from UAS images, image processing was carried out in photogrammetric software packages, which are developed based on computer vision and structure from motion algorithms. The process of image matching, aligning, and bundle block adjustment was performed in SfM software. Exterior orientation parameters were determined by software in the process of aerial triangulation, which is based on least square accurate mathematical models. As a result, three-dimensional structures were obtained from two-dimensional image sequences using the SfM-MVS method. By performing computations in software packages, the following products were generated from images of UAS: 3D dense point clouds, triangulated mesh surfaces, orthomosaics, and digital elevation models (DSMs and DTMs).

A total of 16 photogrammetric projects (with different flight heights and GCP configuration) were processed using three different commercial photogrammetric 3D reconstruction software packages, namely Agisoft PhotoScan Professional version 1.4.3 [56], Pix4Dmapper version 4.3.31 [57], and 3Dsurvey version 2.7.0 [58]. The purpose of processing in different software packages was to analyze, compare, and evaluate the influence of computer applications on the accuracy of products. In order to obtain similar products, in the workflow of all the three software packages, full keypoint extraction and optimal processing options were adopted. Although extremely high processing options are available, they are not recommended for mapping purposes of large data. The SfM-MVS workflow implemented in Agisoft PhotoScan is summarized in the following paragraphs. The specifics of this workflow slightly vary in the three software packages, but a clear commonality exists. Image processing was performed in the following steps.

In the first step, the project was created, the reference coordinate system was chosen, and the images along with their EXIF metadata, including intrinsic camera parameters, were imported in the project workspace. In the next step, the images were aligned by identifying and matching features between overlapping images. The alignment step in PhotoScan comprises three phases. First, features (keypoints) are detected by applying a feature detection algorithm. After locating keypoints in neighboring images, matching keypoints are identified, and inconsistent matches are removed. In the third stage, 3D geometry of the scene and camera parameters (focal length, radial lens distortions, and positions of the principal point) are solved simultaneously using a bundle-adjustment algorithm. In the alignment step, the accuracy was set to “high”, and limits were not specified for the key point and tie point parameters because defining an upper limit for these parameters may cause missing in some parts of the point cloud model and affect the comparison with the other software. At this stage, which is the crucial step in the SfM workflow, the camera position and orientation corresponding to each photo were estimated, and a sparse point cloud model was generated.

After generating the sparse point cloud, the points with the highest reprojection error were removed using the gradual selection option. For generating accurately georeferenced products, 3D coordinates of GCPs were imported, and each was marked manually on visible photos. Subsequently, the camera alignment was optimized using the GCPs. To achieve higher accuracy, an optimization process must be performed; this process calculates camera external and internal parameters and corrects the probable image distortions like the bowl effect [56]. The RMSE of bundle adjustment was under 2.5 cm.

Once the camera parameters and the geometry of the output sparse point cloud were optimized, a dense point cloud was generated by applying MVS image matching algorithms, which are based on the estimated camera positions and the calculated depth information [56]. The depth filtering algorithm was used to filter out the erroneous points in the process of dense point cloud generation. This stage, which requires a longer time for processing (depends on the computer processor and RAM), resulted in a highly detailed 3D point cloud. The dense point cloud can be modified and classified prior to exporting or proceeding to the next step.

Following the above step, a 3D polygonal mesh model was generated based on the dense point cloud data and interpolation between points. Subsequently, the texture was built and applied to the mesh model. Polygonal mesh models can be exported in many formats with significantly less data size compared to point clouds. However, generating mesh models are optional and can be skipped, and the digital surface model (DSM) can be produced directly following dense cloud generation.

Subsequently, the DSM was generated from the dense point clouds. DSM can be generated and rasterized from a sparse point cloud, dense point cloud, or mesh model in geographic or planar projection. Since the dense point cloud yields more accurate results, the digital surface model was generated based on the whole dense point cloud data. The three utilized software packages use noise filtering algorithms for the DSM generation. To generate the DTM of the study area, the dense point cloud was first classified into ground and non-ground classes using the automatic and semi-automatic classification algorithms.

For generating high-resolution orthorectified images of the study area, orthomosaics were generated based on the input photos and constructed DSM at 4.0 and 2.5 cm resolutions. Orthorectification can be done based on the DSM or mesh model. The orthorectification process removes the image perspective effects (i.e., tilt, terrain distortions) and creates orthomosaic, which is planimetrically correct. The abovementioned photogrammetric products generated using PhotoScan are illustrated in Figure 2. Additionally, a combined image processing was performed using the images of both flights to study the contribution of integrated image processing on the accuracy of models. Finally, the generated orthomosaics and elevation models were exported to raster format for further analysis.

The processing was performed using a workstation computer with Windows 10 Professional 64-bit operating system, 3.4 GHz Intel processor, and 128 GB RAM. The total processing time for one project was about 2 hours for PhotoScan and Pix4Dmapper, and approximately 10 hours for 3Dsurvey. For comparing the processing time, the same number of images were processed using a PC with a 3.6 GHz processor and 32 GB RAM. With this system, the processing time for PhotoScan as well as Pix4Dmapper was about 6 hours, and for 3Dsurvey, it took about 20 hours.

2.3. Accuracy assessment

To achieve the aim of the research, comparative absolute and relative accuracy assessment between the derived data and the accurate field measurements was performed. The absolute accuracy assessment in this research is based on CPs that had been accurately measured using ground-based survey methods and had not been involved in the least-squares bundle adjustment and orientation calculation process. The relative accuracy assessment deals with the inter-relational performance of different methods.

Accuracy evaluation was performed based on RMSE because this is the most common metric used in geospatial accuracy analysis, and the new ASPRS standard was also presented in this metric. The errors in RMSE are squared before averaging; therefore, it gives relatively higher weights to large errors. With this in mind, it is better to use the RMSE rather than the mean absolute error (MAE) in such studies. In surveying, RMSE is often preferred to avoid undesirable large errors [2, 11, 59].

Since errors in UAS-SfM-based surveying usually occur in elevations and vertical uncertainty is the primary concern in the literature, this research mainly focuses on vertical accuracy. For vertical accuracy assessment, two sets of CPs (vegetated and non-vegetated) were measured directly on the ground without marking them. A total of 200 CPs (located within and outside of GCP polygons) were surveyed, 100 of which are located in vegetated and 100 in non-vegetated terrain. From the 100 CPs located on the bare surface, 7 of them were marked on the ground and used for horizontal and vertical accuracy assessment, and the rest (unmarked) were used for only vertical accuracy assessment. Accuracy analysis was performed separately on the bare surface and vegetated landcover. Although photogrammetric software packages calculate and provide the horizontal and vertical accuracy assessment report based on the identified GCPs and CPs, the reports cannot satisfy the user. Therefore, the accuracy analysis and evaluation of the products were performed from the end user's point of view.

Linear RMSE of each coordinate, Easting (X), Northing (Y), and elevation (Z), as well as the horizontal (XY), was calculated for each marked checkpoint. Horizontal accuracy assessment was performed on orthomosaics, and then by comparing the coordinates to the actual surveyed (GNSS) coordinates, RMS errors (RMSEX, RMSEY, and RMSEXY) were calculated using the Equation 1 and 2 [2, 11, 54]:

$$RMSE_X = \sqrt{\frac{\sum_{i=1}^{n}(X_{Oi} - X_{GNSSi})^2}{n}} \quad (1)$$

$$RMSE_Y = \sqrt{\frac{\sum_{i=1}^{n}(Y_{Oi} - Y_{GNSSi})^2}{n}} \quad (2)$$

where n is the number of tested CPs; X_{Oi} and Y_{Oi} are X and Y coordinates measured in the orthomosaic for the ith CP; X_{GNSSi} and Y_{GNSSi} are X and Y coordinates measured with the use of RTK GNSS for the ith CP (Equation 3).

$$RMSE_{XY} = \sqrt{RMSE_X{}^2 + RMSE_Y{}^2} \quad (3)$$

For the seven check points, vertical accuracy was calculated in two methods. In the first method, the horizontal positions of CPs were considered from the orthomosaic, and the height value was derived from the grid DSM, and by comparing to the GNSS measurements, $RMSE_{ZO}$ was calculated (Equation 4).

$$RMSE_{ZO} = \sqrt{\frac{\sum_{i=1}^{n}(Z_{Oi} - Z_{GNSSi})^2}{n}} \quad (4)$$

where Z_{Oi} is the elevation in the ith CP obtained from the DSM, considering its X and Y coordinates measured on the orthomosaic; Z_{GNSSi} is the Z coordinate of the ith CP measured with the GNSS.

This approach was adopted as it would be the process that a user would determine the elevation of a point identified on the orthomosaic. However, to some extent, the above method mitigates the effect of horizontal errors. Therefore, the second method used to assess the vertical accuracy was to calculate the elevation difference between DSM and GNSS measurements, while the horizontal positions of CPs were considered directly from the GNSS measurements. In the second method, the RMSEZD was calculated as using Equation 5, which the errors of all vegetated and non-vegetated unmarked CPs were also calculated using this method.

$$RMSE_{ZD} = \sqrt{\frac{\sum_{i=1}^{n}(Z_{Di} - Z_{GNSSi})^2}{n}} \quad (5)$$

where Z_{Di} is the elevation in the ith CP, derived from the DSM, while its X and Y coordinates, measured with the GNSS; and Z_{GNSSi} is the Z coordinate of the ith CP surveyed with the GNSS.

The vertical RMS errors of all vegetated and non-vegetated 200 unmarked CPs were calculated using the second method. Following the calculations, accuracy tables were prepared, and relative frequency histograms of error distribution and scatter plots of elevations were plotted to analyze the correlation and linear association between different survey methods. The R programming language was used to analyze and plot not only the histograms and linear regression models, but also the correlation matrices, including distribution histograms along with the fitted normal density curves, bivariate scatter plots containing a fitted regression model, correlation ellipses, and correlation coefficient values to provide a statistical presentation of data. The charts plotted in R, significantly facilitate the pairwise comparisons. Finally, the obtained accuracies were compared with the ASPRS [54] positional accuracy standard for digital geospatial data.

3. Results and discussion

3.1. Absolute accuracy analysis and evaluation of results

Several factors influence the accuracy of a DSM derived from UAS images, such as flight height, distance to the nearest GCP, image overlap, topography, surface structure, and varying contrast in images [11, 52, 60–66]. In this study, the first two factors were investigated. The following sections present the results of horizontal and vertical accuracy assessment of CPs calculated based on RMSE equations discussed in Section 2.3.

3.1.1. Horizontal and vertical accuracy assessment based on marked CPs

Horizontal errors of orthomosaics in the X direction, Y direction, and radial direction (XY) were calculated for all projects based on 7 marked CPs. The error statistics of one project are given as an example in Table 2. Complete tables are given in the Table 3-6.

Table 2. Horizontal and vertical error statistics of orthomosaics and DSMs derived from 170 m AGL nadir images, processed with 10 GCPs and assessed with 7 GNSS CPs. All values are in meters.

	PhotoScan				Pix4Dmapper				3Dsurvey			
	X	Y	Z_O	Z_D	X	Y	Z_O	Z_D	X	Y	Z_O	Z_D
Min	-0.007	-0.029	-0.016	-0.016	-0.043	-0.014	-0.033	-0.034	-0.029	-0.015	-0.134	-0.134
Max	0.053	0.021	0.108	0.108	0.048	0.068	0.068	0.068	0.018	0.074	0.107	0.107
Mean	0.010	-0.005	0.040	0.040	0.011	0.014	0.027	0.026	0.004	0.025	-0.055	-0.055
MAE	0.014	0.018	0.045	0.044	0.027	0.020	0.036	0.036	0.012	0.032	0.086	0.085
RMSE	0.022	0.020	0.054	0.053	0.031	0.030	0.040	0.040	0.015	0.042	0.092	0.092
$RMSE_{XY}$	0.029				0.044				0.045			
$RMSE_{XYZ}$	0.061				0.059				0.102			

Table 3. Horizontal and vertical error statistics of orthomosaics and DSMs derived from 100 m AGL nadir images, processed with 5 GCPs and assessed with 7 GNSS CPs. All values are in meters.

	PhotoScan				Pix4Dmapper				3Dsurvey			
	X	Y	Z_O	Z_D	X	Y	Z_O	Z_D	X	Y	Z_O	Z_D
Min	-0.018	0.006	-0.216	-0.222	-0.018	0.009	-0.151	-0.151	-0.053	0.023	-0.088	-0.108
Max	0.030	0.052	0.157	0.157	0.037	0.051	0.100	0.099	0.052	0.166	0.123	0.123
Mean	0.005	0.018	-0.023	-0.024	0.004	0.024	-0.003	-0.004	0.012	0.078	-0.014	-0.025
MAE	0.017	0.018	0.098	0.097	0.014	0.024	0.083	0.081	0.040	0.078	0.075	0.070
RMSE	0.018	0.023	0.125	0.125	0.018	0.028	0.096	0.095	0.042	0.093	0.079	0.076
RMSEXY	0.029				0.033				0.102			
RMSEXYZ	0.128				0.101				0.129			

Table 4. Horizontal and vertical error statistics of orthomosaics and DSMs derived from 100 m AGL nadir images, processed with 10 GCPs and assessed with 7 GNSS CPs. All values are in meters.

	PhotoScan				Pix4Dmapper				3Dsurvey			
	X	Y	Z_O	Z_D	X	Y	Z_O	Z_D	X	Y	Z_O	Z_D
Min	-0.008	-0.015	-0.151	-0.146	-0.013	-0.029	-0.024	-0.024	-0.038	-0.027	-0.139	-0.139
Max	0.038	0.087	0.008	0.003	0.034	0.056	0.076	0.075	0.016	0.060	0.190	0.190
Mean	0.007	0.022	-0.053	-0.056	0.006	0.016	0.020	0.019	-0.005	0.025	-0.018	-0.018
MAE	0.011	0.027	0.055	0.056	0.012	0.032	0.038	0.037	0.014	0.033	0.086	0.086
RMSE	0.016	0.036	0.073	0.073	0.016	0.036	0.046	0.045	0.019	0.040	0.104	0.104
RMSEXY	0.040				0.039				0.044			
RMSEXYZ	0.083				0.060				0.113			

Table 5. Horizontal and vertical error statistics of orthomosaics and DSMs derived from 170 m AGL nadir images, processed with 5 GCPs and assessed with 7 GNSS CPs. All values are in meters.

	PhotoScan				Pix4Dmapper				3Dsurvey			
	X	Y	Z_O	Z_D	X	Y	Z_O	Z_D	X	Y	Z_O	Z_D
Min	-0.020	-0.014	-0.138	-0.138	-0.036	-0.017	-0.172	-0.175	-0.036	0.003	-0.268	-0.268
Max	0.030	0.013	0.027	0.027	0.070	0.093	0.071	0.071	0.137	0.099	0.055	0.055
Mean	0.005	0.002	-0.055	-0.055	0.008	0.035	-0.017	-0.019	0.017	0.052	-0.083	-0.081
MAE	0.015	0.011	0.063	0.063	0.021	0.040	0.070	0.071	0.047	0.052	0.105	0.102
RMSE	0.017	0.011	0.074	0.075	0.032	0.048	0.085	0.087	0.062	0.064	0.139	0.138
RMSEXY	0.020				0.058				0.089			
RMSEXYZ	0.077				0.103				0.165			

Table 6. Horizontal and vertical error statistics of orthomosaics and DSMs derived from the merged process of 100 and 170 m AGL nadir images and assessed with 7 GNSS CPs in Photoscan. All values are in meters.

	X	Y	Z_O	Z_D
Min	-0.013	-0.006	-0.086	-0.086
Max	0.037	0.054	0.029	0.029
Mean	0.002	0.019	-0.025	-0.025
MAE	0.013	0.021	0.037	0.036
RMSE	0.016	0.027	0.047	0.047
RMSEXY	0.032			
RMSEXYZ	0.057			

The results showed that horizontal accuracy was not affected by flight height; however, it was significantly affected by the number and distribution of GCPs. The results of Pix4Dmapper and 3Dsurvey showed that accuracy was improved by increasing the number of GCPs. Nevertheless, by increasing the number of GCPs, no improvement was observed in the horizontal accuracy of the results processed by PhotoScan. The maximum horizontal and vertical errors indicate the error of points outside of GCP polygon. Since the results show that the horizontal errors are in the level of 1-1.5 × GSD, the values of ZO and ZD in the above table demonstrate that vertical accuracy was not affected by the horizontal error.

To summarize the horizontal accuracy of PhotoScan, from both flight heights, orthomosaics were produced with RMSEX and RMSEY of ~2 cm, and horizontal accuracy (RMSEXY) of ~3 cm. According to the American Society for Photogrammetry and Remote Sensing (ASPRS) positional accuracy standards for digital geospatial data [54], the horizontal accuracy obtained from the images of 100 m AGL with 2.5 cm GSD meets the ASPRS 2014 standard horizontal accuracy class RMSEx and RMSEY of 2.5 cm and RMSEr (the horizontal linear RMSE) of 3.5 cm for normal error distribution. The RMSEXY matches 6.1 cm accuracy at 95% confidence level. According to Class 1 of the legacy ASPRS map standard 1990 [67], the equivalent map scale for the achieved horizontal accuracy is 1:100. Similarly, the horizontal accuracy achieved from the images of 170 m AGL with 4.0 cm GSD meets the ASPRS 2014 standard horizontal accuracy class RMSEX and RMSEY of 5.0 cm and RMSEr of 7.1 cm for normal error distribution, and the horizontal accuracy at 95% confidence level is 12.2 cm. Referring to Class 1 of ASPRS 1990, the corresponding map scale for the achieved horizontal accuracy is 1:200.

The achieved horizontal accuracies in this study agree with the findings of Agüera-Vega et al. [11]; Bennassi et al. [68]; Cryderman et al. [69]; Fernández et al. [40]; Gerke & Przybilla [51]; Gindraux [62]; Gonçalves & Henriques [47]; Jaud et al. [59]; Martínez-Carricondo et al. [2]; Rehak & Skaloud [70]; Reshetyuk & Mårtensson [55]; Whitehead & Hugenholtz,[71]; and Wierzbicki et al. [72]. However, some studies achieved lower accuracy from closer ranges. For instance, from a flight height of about 50 m AGL, Pérez et al. [73] and Lucieer et al. [41] obtained RMSEXY of 7.2 and 7.0 cm, respectively. Similarly, Coveney and Roberts [38] obtained RMSEXY of 7.6 cm from 90 m height AGL. Sanz-Ablanedo et al. [44]

and Hill [74] achieved horizontal accuracy of 8.6 and 10 cm, respectively. Hastaoğlu et al. [75, 76] achieved horizontal accuracy of 1-2 × GSD in their studies.

The double block combined processing of the images taken from the cross flights (100 and 170 m heights AGL processed with 5 GCP) showed remarkable 3D accuracy improvement (~2 cm). Nevertheless, horizontal accuracy was not improved significantly. PhotoScan outperformed both Pix4Dmapper and 3Dsurvey in horizontal accuracy. It is worth to mention that vertical accuracy evaluation based on the 7 CPs were performed not only to assess the horizontal accuracy but also to find the effect of the horizontal error on the vertical accuracy. Vertical accuracy (RMSEZD) was evaluated comprehensively based on 200 CPs, which is given in the following section.

3.1.2. Vertical accuracy assessment based on 200 unmarked CPs

As discussed in previous sections, according to literature, horizontal accuracy is not the main concern in UAS-SfM-based surveying. In UAS-SfM-derived DSMs, the major errors usually occur in Z values. With this in mind, horizontal accuracy was assessed based on 7 CPs, and given the importance of elevation in topographic mapping, vertical accuracy assessment was performed based on 200 CPs in vegetated and non-vegetated areas. The vertical accuracy of non-vegetated and vegetated land cover was evaluated separately. The results of the accuracy assessment and statistical analysis are presented in the following sections. The vertical error statistics are given in Table 7 and Table 8.

Table 7. Vertical error statistics of DSMs derived from 100 m AGL nadir images, processed with 5 & 10 GCPs, and assessed with 100 GNSS CPs. All values are in meters.

	PhotoScan		Pix4Dmapper		3Dsurvey	
	5 GCP	10 GCP	5 GCP	10 GCP	5 GCP	10 GCP
Min	-0.344	-0.165	-0.245	-0.104	-0.190	-0.270
Max	0.163	0.030	0.123	0.101	0.123	0.222
Mean	-0.004	-0.051	0.011	0.002	-0.059	-0.059
MAE	0.075	0.053	0.068	0.031	0.076	0.118
RMSE	0.102	0.066	0.085	0.039	0.091	0.137

Table 8. Vertical error statistics of DSMs derived from 170 m AGL nadir images, processed with 5, 10, and without GCPs, and assessed with 100 GNSS CPs. All values are in meters.

	PhotoScan			Pix4Dmapper			3Dsurvey		
	5 GCP	10 GCP	without GCP	5 GCP	10 GCP	without GCP	5 GCP	10 GCP	without GCP
Min	-0.324	-0.080	-1.633	-0.375	-0.302	-1.264	-0.481	-0.190	-1.034
Max	0.091	0.203	-0.577	0.394	0.330	0.320	0.266	0.107	0.463
Mean	-0.044	0.031	-0.974	0.016	0.031	-0.320	-0.080	-0.042	-0.008
MAE	0.055	0.048	0.974	0.077	0.050	0.398	0.100	0.071	0.293
RMSE	0.076	0.059	1.015	0.103	0.071	0.514	0.133	0.084	0.356

Table 7 compares the elevation error statistics of DSMs derived from 100 m AGL nadir images processed with 5 and 10 GCPs using the three software. The results of PhotoScan and Pix4Dmapper clearly showed the impact of GCP on the accuracy, where the highest elevation accuracy was achieved by Pix4Dmapper (3.9 cm) and PhotoScan (6.6 cm) using 10 GCPs. Georeferencing using 10 GCPs resulted in 3.6 and 4.6 cm improvement in accuracy comparing to 5 GCPs. On the contrary, in 3Dsurvey, the RMS error increased by increasing the number of GCPs.

As Table 4 demonstrates, the errors in DSMs derived from images of 170 m show the same trend for PhotoScan and Pix4Dmapper, where vertical accuracy increased by doubling the GCP numbers. However, PhotoScan shows higher accuracy than Pix4Dmapper. Contrary to 3Dsurvey's results at 100 m AGL, accuracy was increased in the 10 GCP schemes of 170 m AGL; however, it is still lower than PhotoScan and Pix4Dmapper. The vertical accuracy ranged from 0.356 m to 1.015 m when processed without GCP.

For the ease of interpretation, comparison, and correlation analysis, relative frequency histograms of errors were plotted in classes of 2 cm interval to compare each class to the total number of errors. To measure the linear dependence between SfM DSM elevations and the validation data of DGNSS, correlation analysis was performed based on the Pearson correlation method, which is the most common technique for measuring the strength of the association between two variables. Pairwise matrices were prepared, and correlation coefficients were computed. Figure 5 shows relative frequency histograms of elevation difference between UAS-SfM and DGNSS elevations along with the fitted linear regression models for the projects processed with 5 GCPs.

For relative accuracy analysis of SfM DSMs generated using three different software packages, correlation matrices were plotted using the R programming language to investigate the relationship between multiple variables (DGNSS validation elevations, Agisoft PhotoScan DSM elevations, Pix4Dmapper DSM

elevations, and 3Dsurvey DSM elevations) simultaneously. A chart of the correlation matrix was plotted for each project. In the correlation matrix diagram, the distribution histogram of each variable (elevation) along with a fitted normal density curve is shown on the diagonal. The bivariate scatter plots, including a fitted line and correlation ellipses, are displayed at the bottom of the diagonal. Correlation coefficient values are given above the diagonal. The chart combines the statistical presentation of data, which facilitates pairwise comparison and measuring the linear association between two variables as well as the visual test for bivariate normality. Pairwise elevation correlation matrix for projects processed with 5 GCPs are given in Figure 6. Figure 7 shows relative frequency histograms of elevation difference between UAS-SfM and DGNSS elevations with the fitted linear regression models for the projects processed with 10 GCPs.

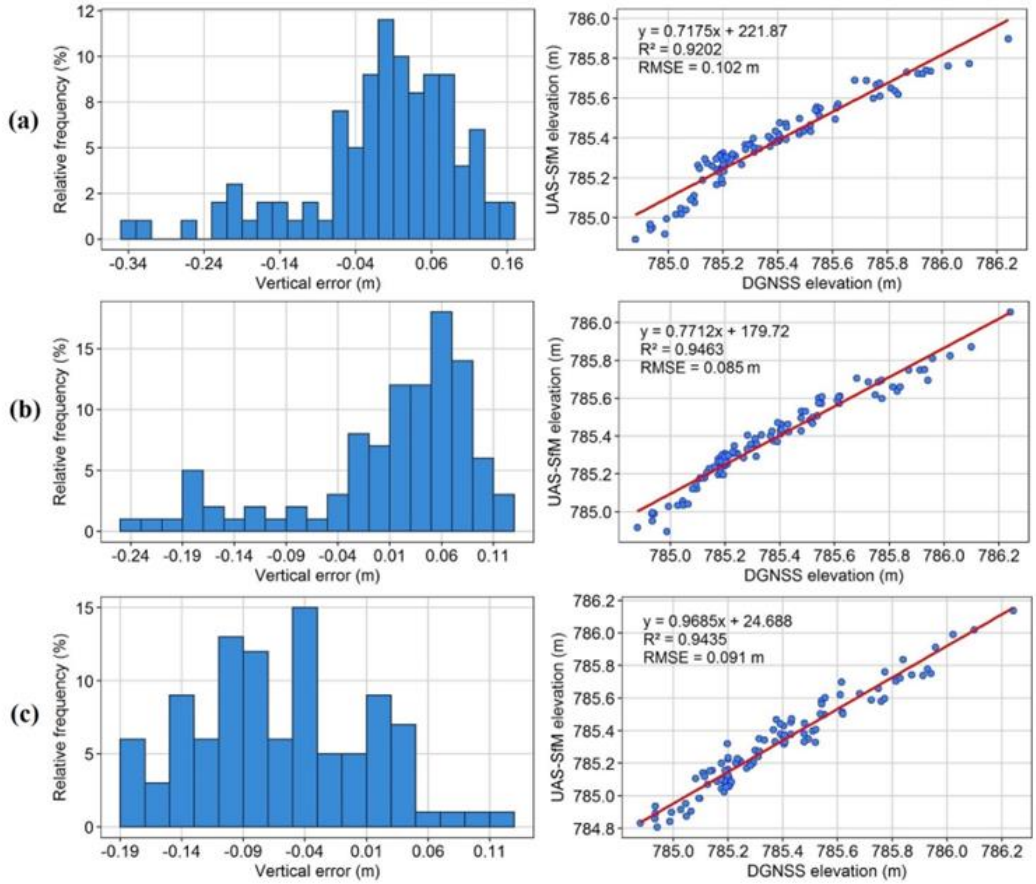

Figure 5. Relative frequency histogram of non-vegetated vertical errors and scatter plot of correlation between UAS-SfM and DGNSS elevations. UAS-SfM DSM derived from 100 m AGL nadir images, processed with 5 GCPs using (a) PhotoScan, (b) Pix4Dmapper, and (c) 3Dsurvey.

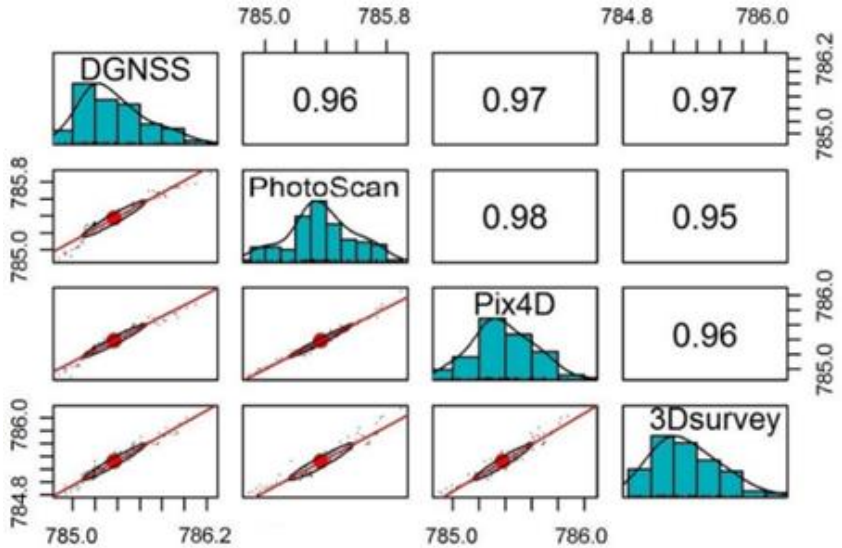

Figure 6. Correlation matrix plot with bivariate scatter plots, distributions, and correlation ellipses of DGNSS non-vegetated elevations and UAS-SfM DSM elevations derived from 100 m AGL nadir images, processed with 5 GCPs.

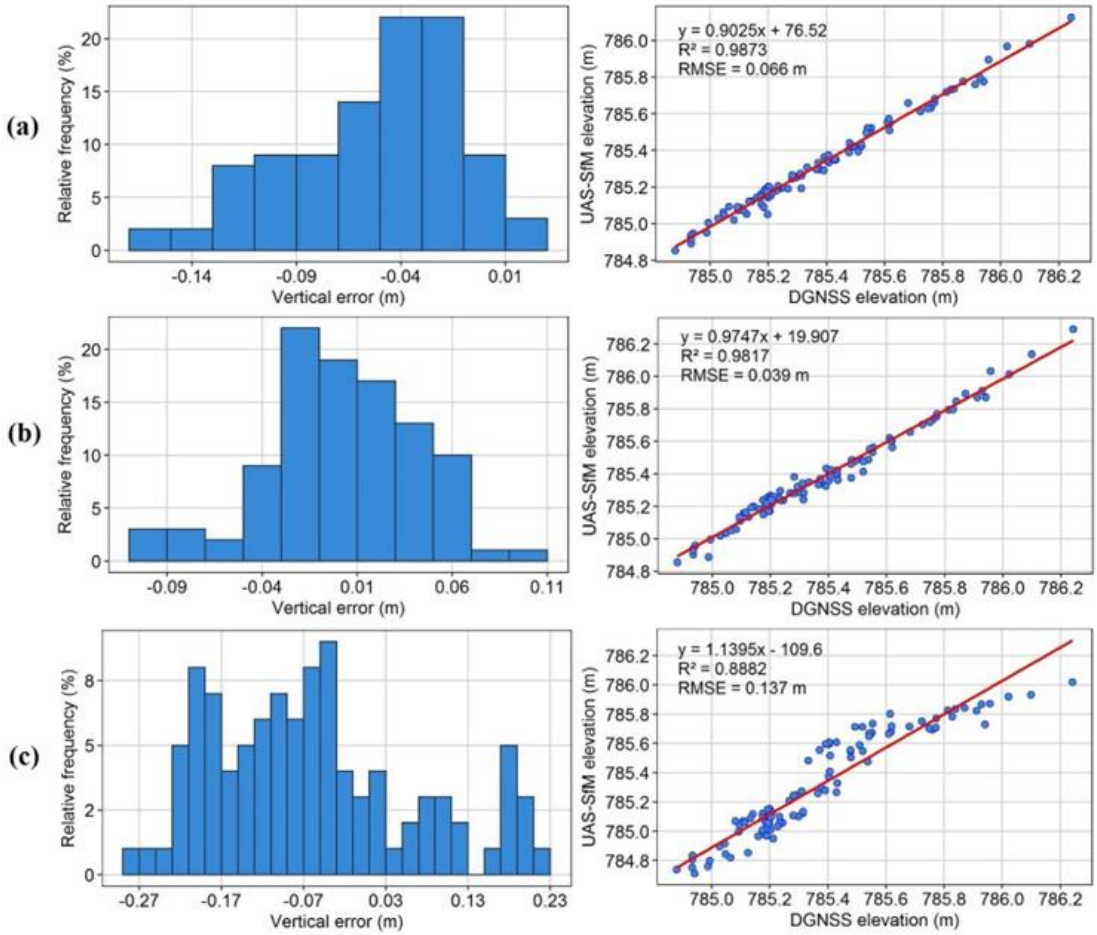

Figure 7. Relative frequency histogram of non-vegetated vertical errors and scatter plot of correlation between UAS-SfM and DGNSS elevations. UAS-SfM DSM derived from 100 m AGL nadir images, processed with 10 GCPs using (a) PhotoScan, (b) Pix4Dmapper, and (c) 3Dsurvey.

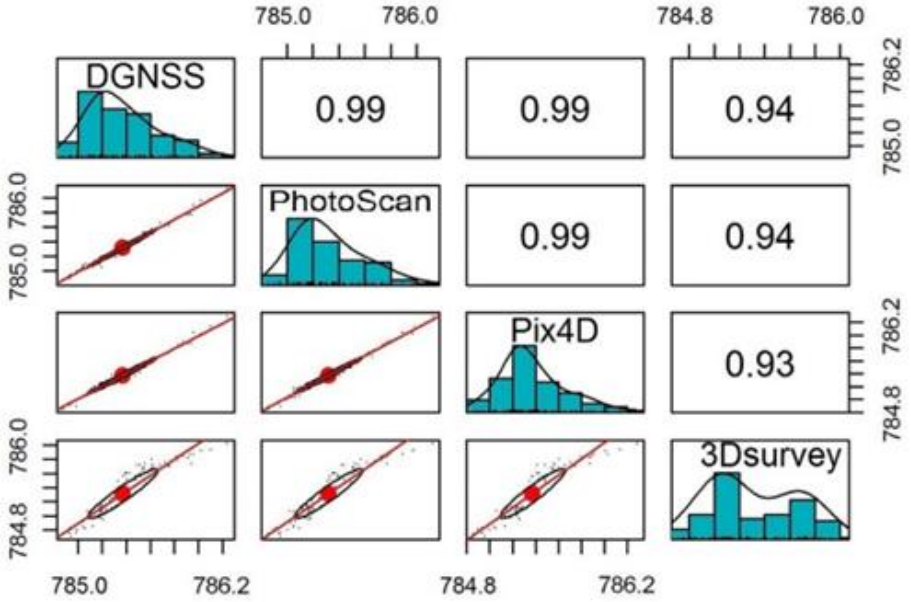

Figure 8. Correlation matrix plot with bivariate scatter plots, distributions, and correlation ellipses of DGNSS non-vegetated elevations and UAS-SfM DSM elevations derived from 100 m AGL nadir images, processed with 10 GCPs.

Figure 7 shows pairwise elevation correlation matrix for the projects processed with 10 GCPs. Figures 5 to 8 illustrate the relative frequency histograms of vertical error and pairwise correlation of elevations for the DSMs derived from images collected at 100 m height (Figure 9-12 for the DSMs derived from 170 m AGL images). The figures indicate that there is a high positive linear correlation between DGNSS and SfM DSM elevations. For the 5 GCP scheme, as RMSE values for PhotoScan, Pix4Dmapper, and 3Dsuvey are very close (10.2, 8.5, and

9.1 cm, respectively), they show almost the same trend, and there is no significant difference in correlation. However, histograms show high similarities in error distribution between PhotoScan and Pix4Dmapper. On the other hand, 3Dsurvey shows quite different error distribution and fewer outliers. The results of the 10 GCP scheme showed that vertical accuracy remarkably increased in Pix4Dmapper and PhotoScan. R-squared values in scatter plots also showed a high correlation between the elevations of PhotoScan, Pix4Dmapper, and DGNSS. The minimum and maximum error values decreased, and outliers were significantly reduced in the 10 GCP scheme. However, the result of 3Dsurvey showed higher error values and a relatively weak correlation.

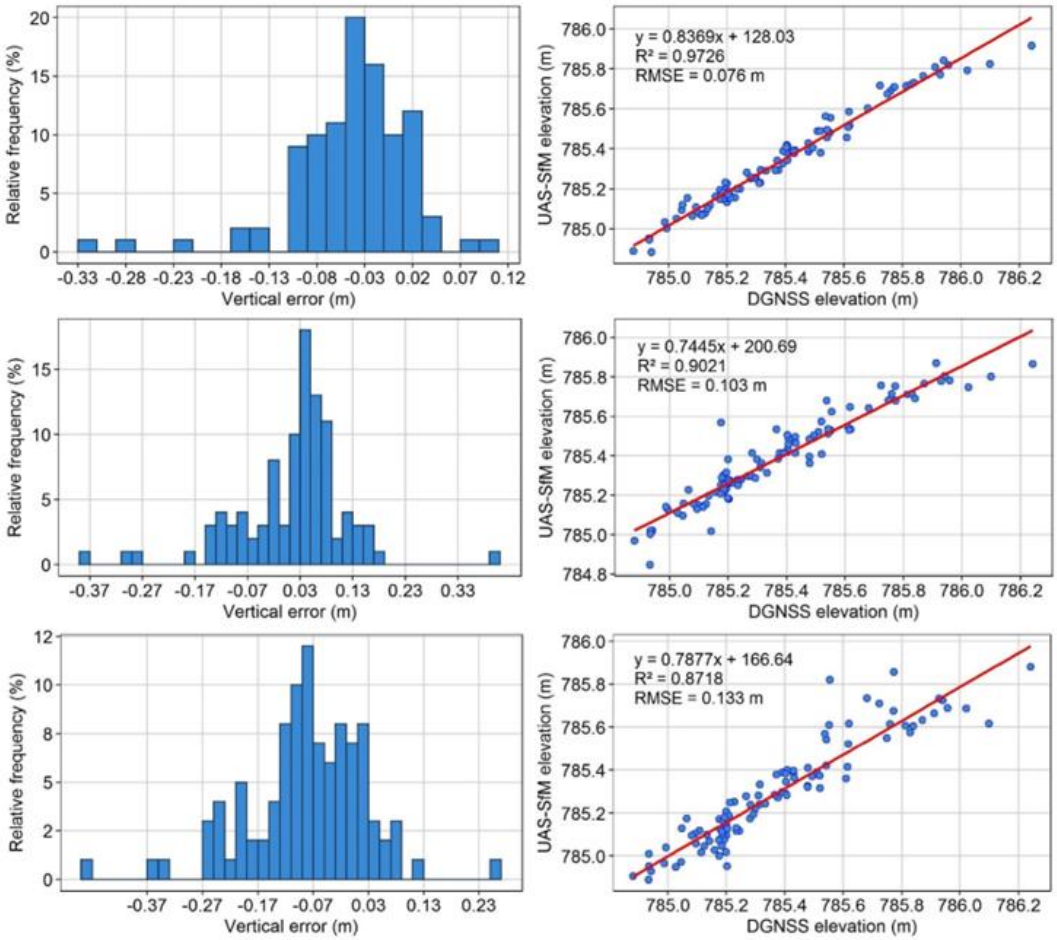

Figure 9. Relative frequency histogram of non-vegetated vertical errors and scatter plot of correlation between UAS-SfM and DGNSS elevations. UAS-SfM DSM derived from 170 m AGL nadir images, processed with 5 GCPs using PhotoScan (top), Pix4Dmapper (middle), and 3Dsurvey (bottom).

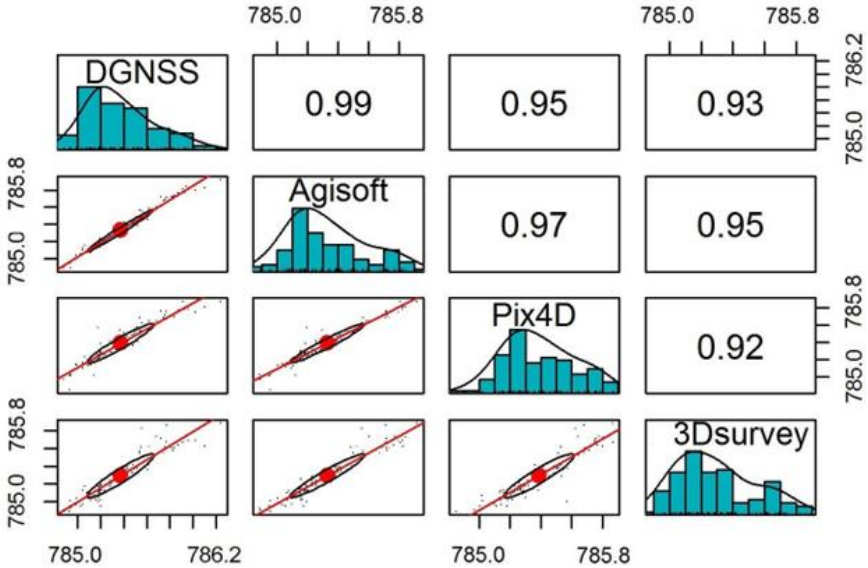

Figure 10. Correlation scatter plot matrix of DGNSS non-vegetated elevations and UAS-SfM DSM elevations derived from 170 m AGL nadir images, processed with 5 GCPs.

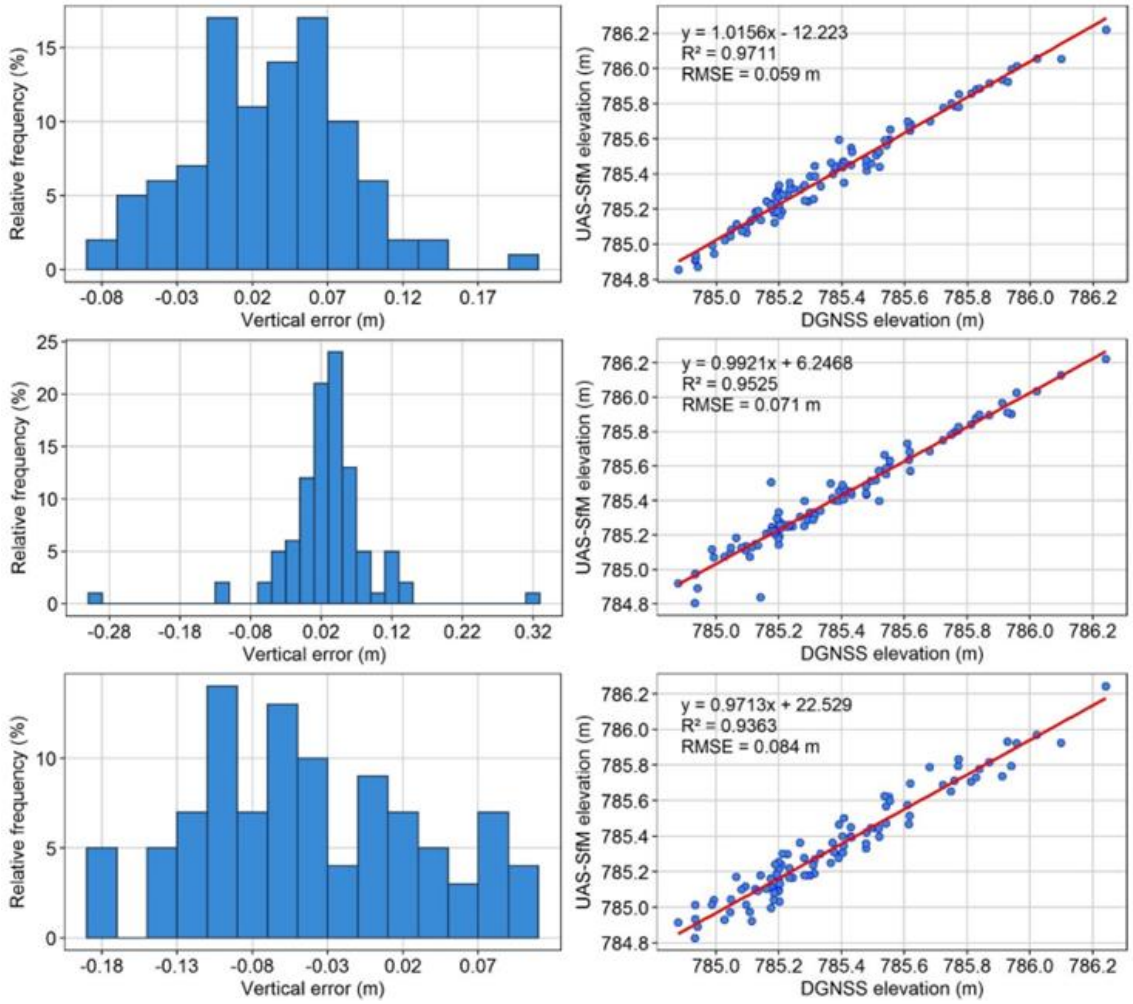

Figure 11. Relative frequency histogram of non-vegetated vertical errors and scatter plot of correlation between UAS-SfM and DGNSS elevations. UAS-SfM DSM derived from 170 m AGL nadir images, processed with 10 GCPs using PhotoScan (top), Pix4Dmapper (middle), and 3Dsurvey (bottom).

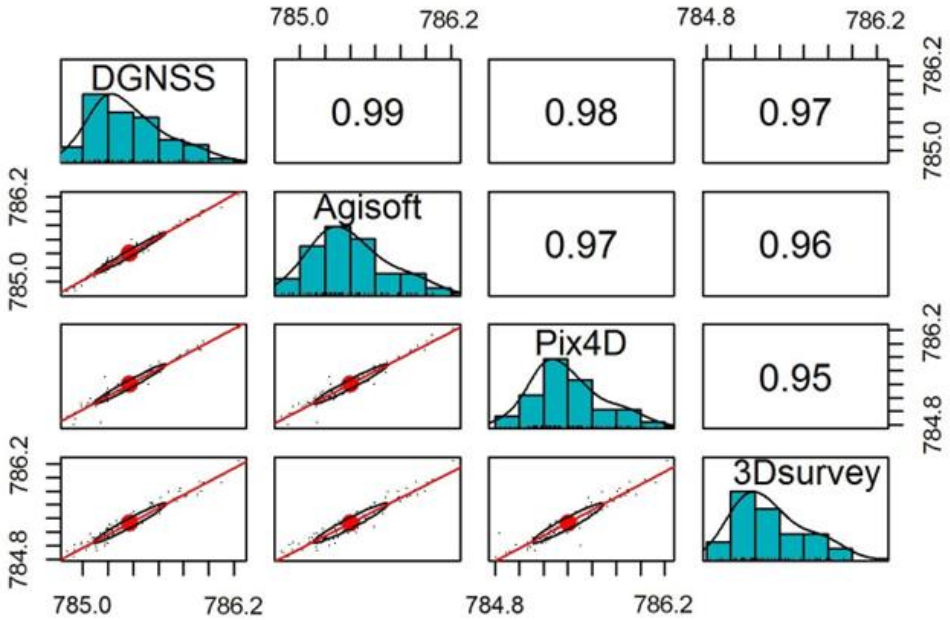

Figure 12. Correlation scatter plot matrix of DGNSS non-vegetated elevations and UAS-SfM DSM elevations derived from 170 m AGL nadir images, processed with 10 GCPs.

The results of statistical analysis illustrate that in 5 GCP scheme, the vertical correlation is weaker, and the number of outliers is higher than the 10 GCP scheme for both projects. For the project 170 m AGL, in the 10 GCP scheme, the error distribution for PhotoScan was almost normal, ranging from -8.0 cm to 20.3 cm with only one

outlier; this is because lightweight drones with fixed wings can maintain overlap at higher altitudes. Similarly, Pix4Dmapper showed a nearly normal distribution ranging from -30.2 cm to 33.0 cm with three outliers. The error distribution in 3Dsurvey ranges from -19.0 to 10.7 cm. PhotoScan and Pix4Dmapper showed higher accuracy and correlation in both GCP schemes; however, 3Dsurvey yielded lower accuracy with a relatively weak correlation.

To sum up, in the non-vegetated area, the highest vertical accuracy of 3.9 cm was achieved from the images of 100 m AGL using 10 GCPs by Pix4Dmapper. This accuracy meets Class 3 (RMSE 5 cm) of ASPRS 2014 absolute accuracy, which the equivalent Class 1 contour interval as per ASPRS 1990 is 15 cm. Since PhotoScan achieved 6.6 cm accuracy, based on the ASPRS standard, this is equivalent to 9.8 cm absolute accuracy at 95% confidence level. From the images of 170 m AGL, the highest achieved accuracy was 5.9 cm by PhotoScan, which agrees with Class 4 (RMSE 10 cm) of ASPRS 2014; accordingly, 95% confidence level is 19.6 cm. The equivalent Class 1 contour interval as per ASPRS 1990 is 30 cm. The achieved vertical results are also consistent with the literature mentioned in the above section. Although the number of GCPs used in the literature varies, the synthesis of results from the literature used in this study indicates that the average vertical accuracy reliability is at the level of 10 cm, which this accuracy agrees with Class 4 of ASPRS 2014.

Using a passive sensor in remote sensing, terrain modeling under densely vegetated areas is difficult and practically not recommended for topographic mapping. However, in sparsely vegetated areas using filtering algorithms or by integrating with terrestrial measurements, topographic data can be provided. Bearing this in mind, the accuracy assessment of the DTMs was carried out on areas covered with grasses and sparse trees. The vertical error distribution histograms, scatter plot of correlations, and matrices are given in the supplementary document (Figure 13-20). According to the ASPRS 2014, vegetated vertical accuracy is an estimate of the vertical accuracy based on the 95% confidence level in vegetated terrain, where vertical errors do not necessarily approximate a normal distribution. The results showed a vertical accuracy of 7 to 11 cm in areas with sparse and low-height vegetation. The results revealed that by increasing the GCP numbers, the vegetated accuracy also increased to some extent. The correlation was also improved using 10 GCPs; nevertheless, some outliers remained, which is normal for vegetated areas.

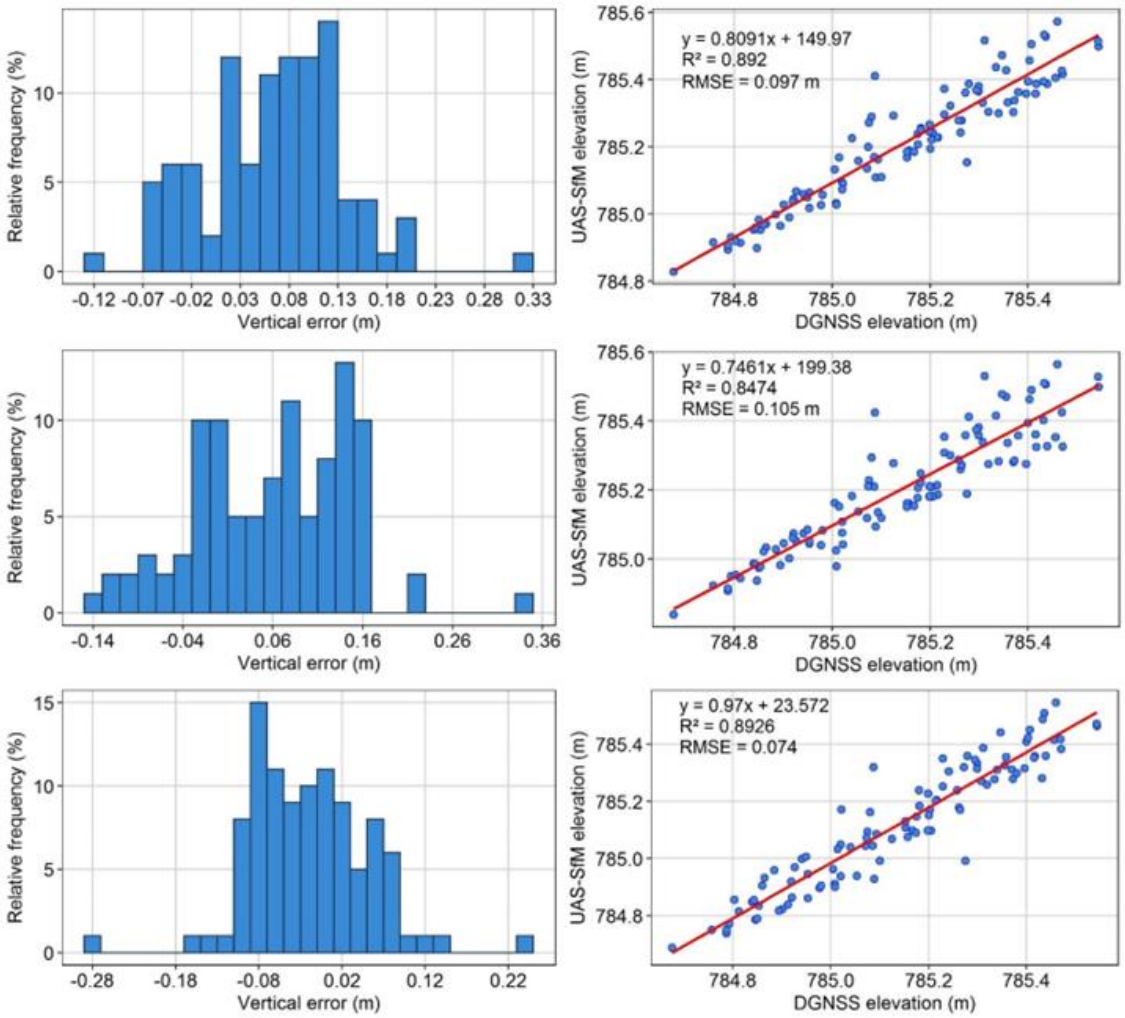

Figure 13. Relative frequency histogram of vegetated vertical errors and scatter plot of correlation between UAS-SfM and DGNSS elevations. UAS-SfM DTM derived from 100 m AGL nadir images, processed with 5 GCPs using PhotoScan (top), Pix4D (middle), and 3Dsurvey (bottom).

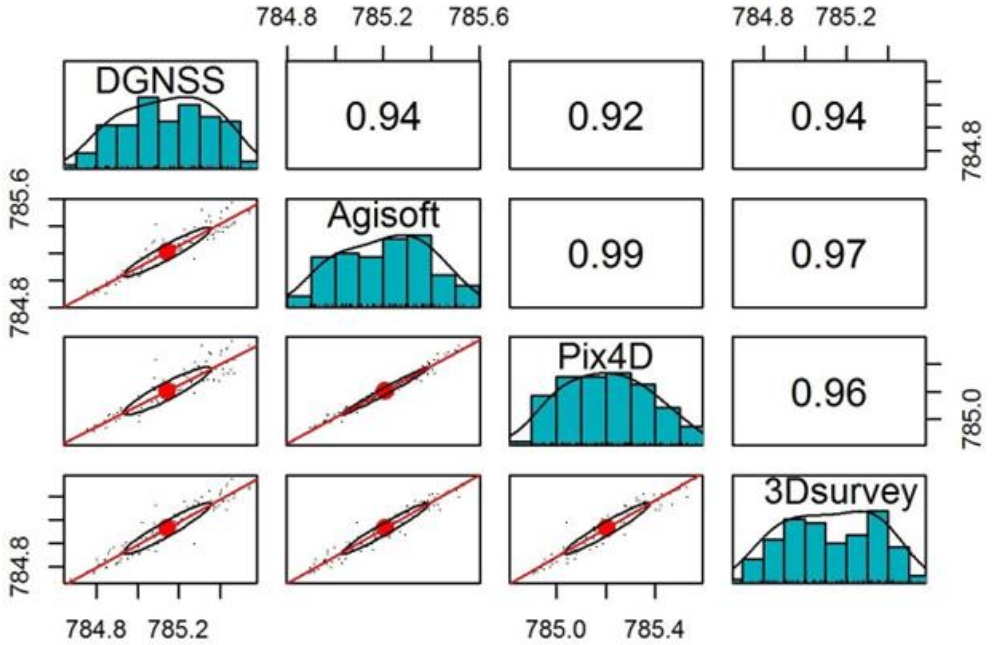

Figure 14. Correlation scatter plot matrix of DGNSS vegetated elevations and UAS-SfM DTM elevations derived from 100 m AGL nadir images, processed with 5 GCPs.

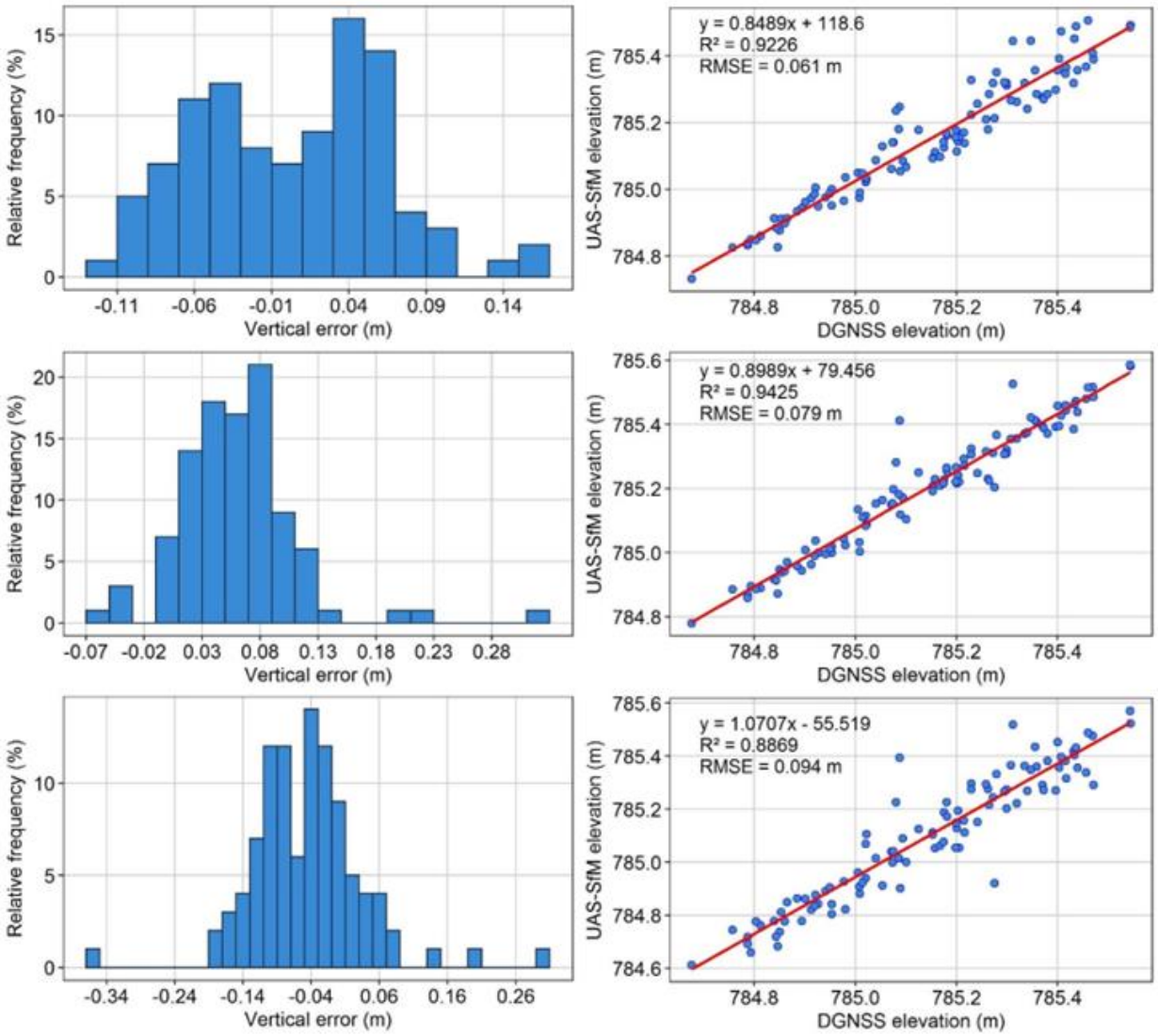

Figure 15. Relative frequency histogram of vegetated vertical errors and scatter plot of correlation between UAS-SfM and DGNSS elevations. UAS-SfM DTM derived from 100 m AGL nadir images, processed with 10 GCPs using PhotoScan (top), Pix4D (middle), and 3Dsurvey (bottom).

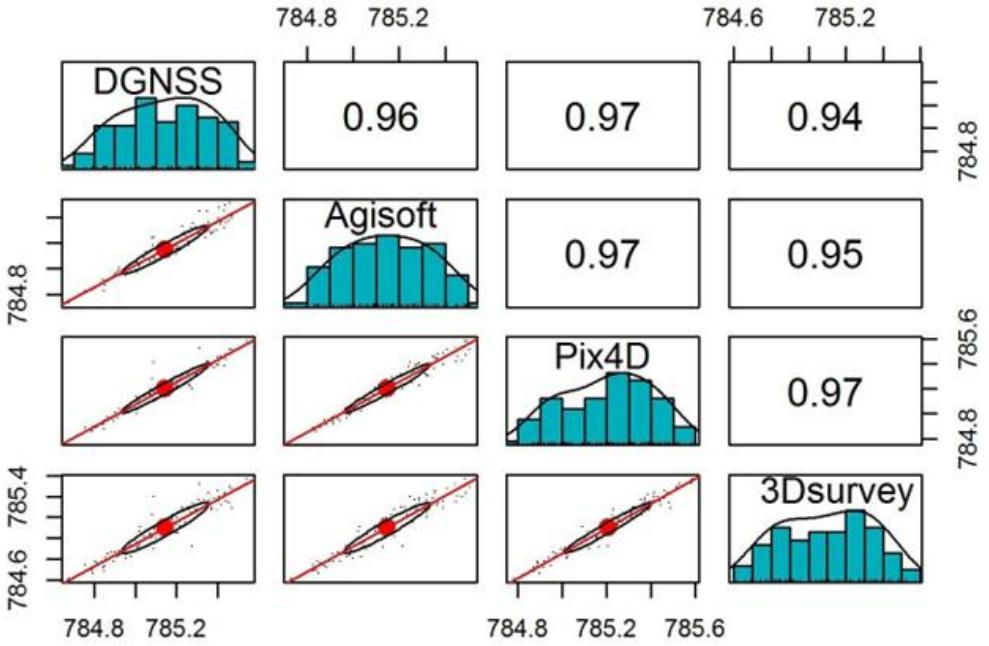

Figure 16. Correlation scatter plot matrix of DGNSS vegetated elevations and UAS-SfM DTM elevations derived from 100 m AGL nadir images, processed with 10 GCPs.

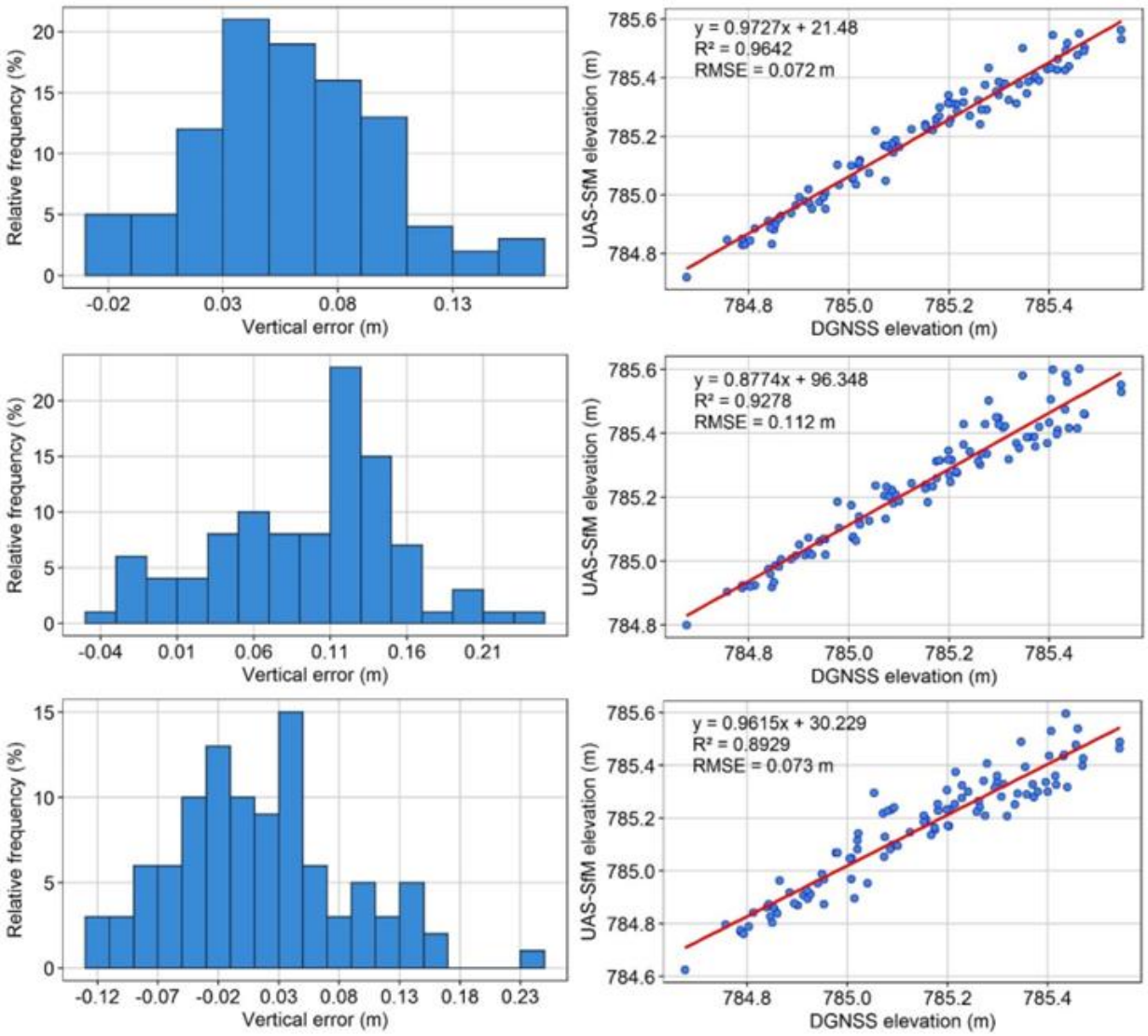

Figure 17. Relative frequency histogram of vegetated vertical errors and scatter plot of correlation between UAS-SfM and DGNSS elevations. UAS-SfM DTM derived from 170 m AGL nadir images, processed with 5 GCPs using PhotoScan (top), Pix4D (middle), and 3Dsurvey (bottom).

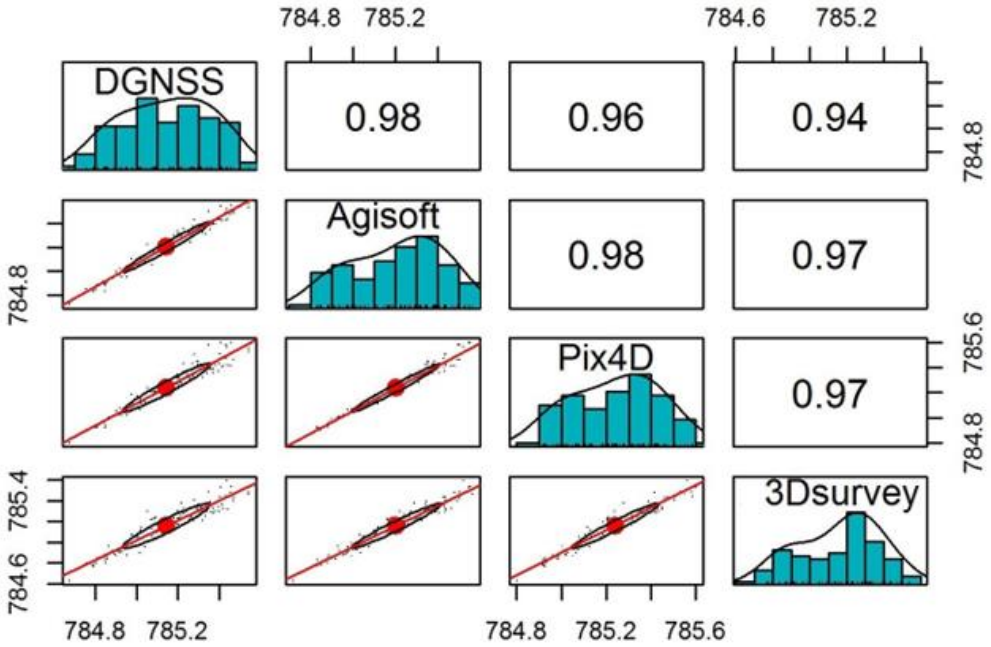

Figure 18. Correlation scatter plot matrix of DGNSS vegetated elevations and UAS-SfM DTM elevations derived from 170 m AGL nadir images, processed with 5 GCPs.

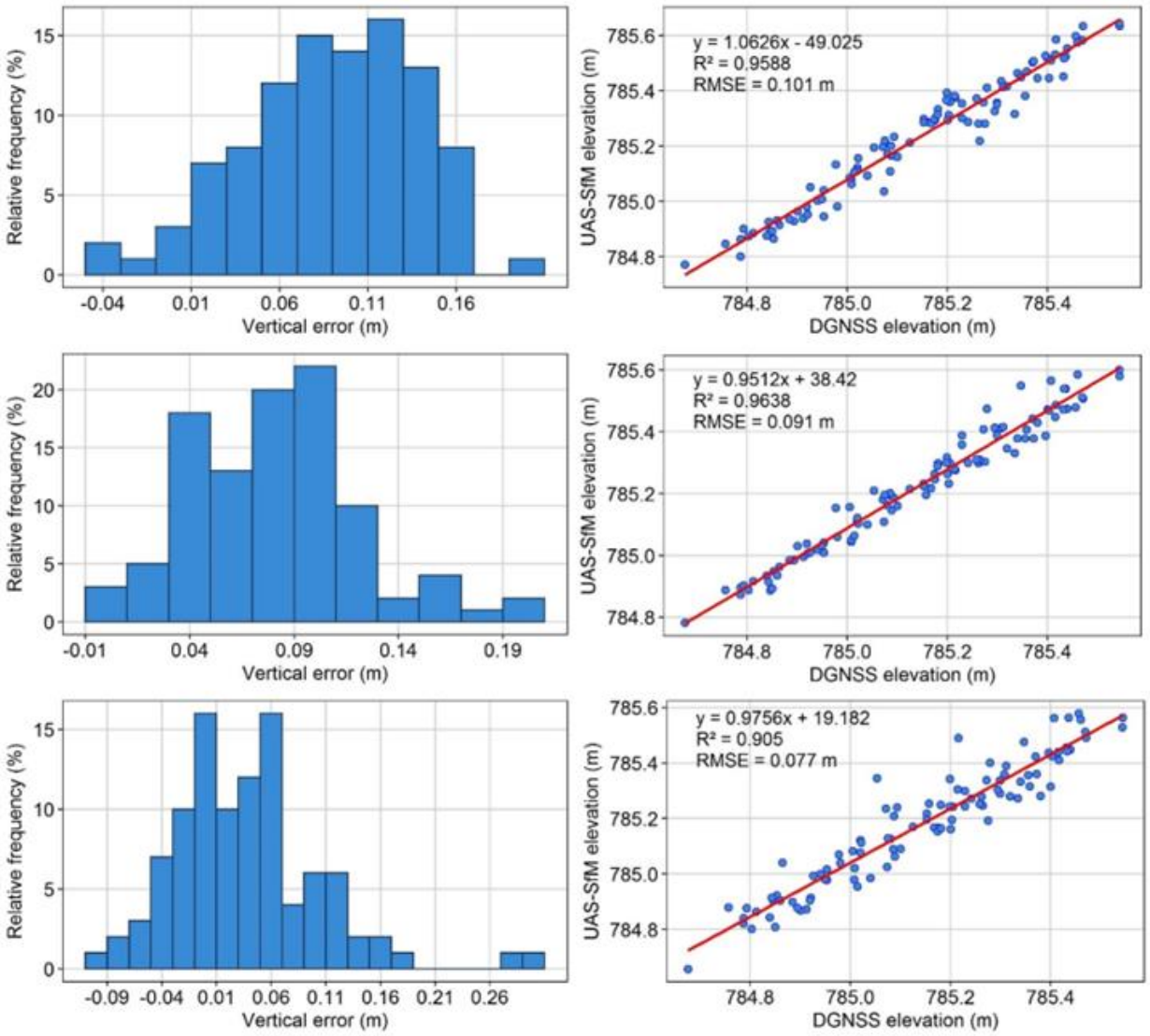

Figure 19. Relative frequency histogram of vegetated vertical errors and scatter plot of correlation between UAS-SfM and DGNSS elevations. UAS-SfM DTM derived from 170 m AGL nadir images, processed with 10 GCPs using PhotoScan (top), Pix4D (middle), and 3Dsurvey (bottom).

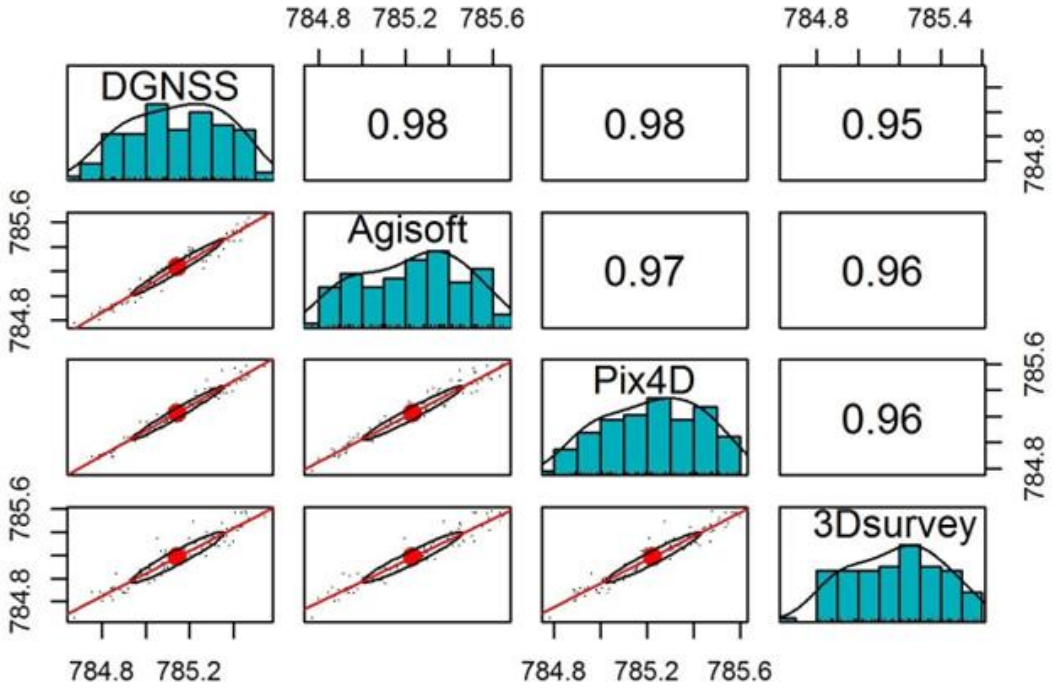

Figure 20. Correlation scatter plot matrix of DGNSS vegetated elevations and UAS-SfM DTM elevations derived from 170 m AGL nadir images, processed with 10 GCPs.

3.1.3. Vertical accuracy of the combined project

To assess the accuracy of the project combined from different flight heights, an integrated image processing was performed by combining images of cross flights. Blocks of 100 m and 170 m AGL nadir images were processed using PhotoScan with 5 GCPs. Figure 21 and Figure 22 demonstrate the histogram and correlation matrix of accuracy analysis for the combined project. By comparing the DSM accuracy of this project with that of projects that were processed individually with 5 GCPs, we can see that in flight 1 (170 m AGL), the error range is from -34 to 16 cm, in flight 2 (100 m AGL) with the same GCP number, errors range from -32 to 9 cm, while in the combined project, the error range is from -15 to 7 cm.

The error histogram of the DSM derived from the combined project (Figure 21) shows a significant improvement in the elevation accuracy. Although the scatter plots of both separately processed projects show high correlation coefficient values, the error distribution histograms show large outliers in both projects. The relative frequency histogram of errors in the combined project shows that outliers were removed, and errors have a nearly normal distribution. Moreover, considering the correlation coefficient and the confidence ellipses (Figure 22), the correlation of the combined project processed with 5 GCPs is comparable with that of projects that were separately processed using 10 GCPs. Figure 22 shows that a high correlation exists between the elevations of the DSM derived from the integrated process and other DSMs that were generated from single flight blocks. The integrated project not only improved accuracy but also resulted in more detail and better 3D models.

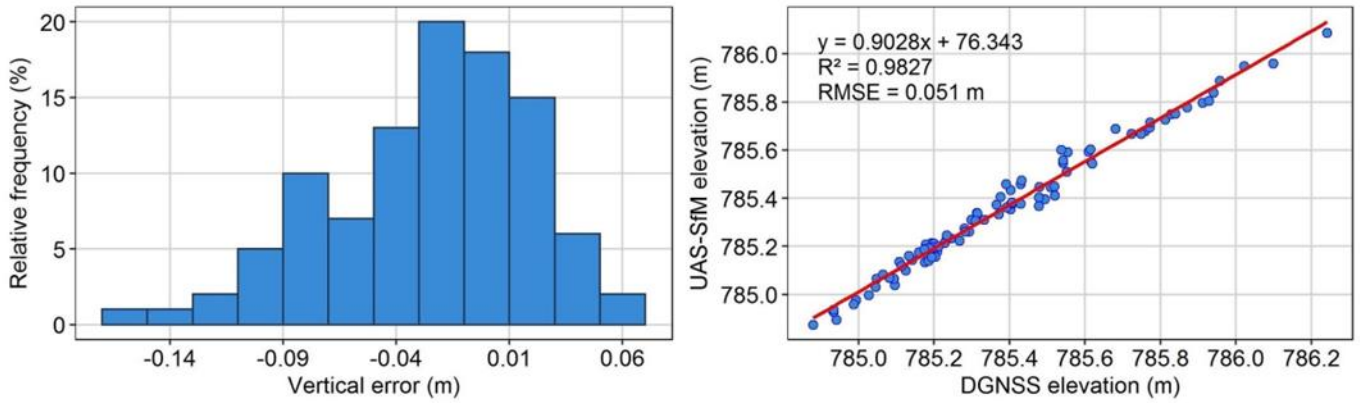

Figure 21. Relative frequency histogram of vertical errors and scatter plot of correlation between UAS-SfM and DGNSS non-vegetated elevations. UAS-SfM DSM derived from the combined process of cross flight nadir images, processed with 5 GCPs using PhotoScan.

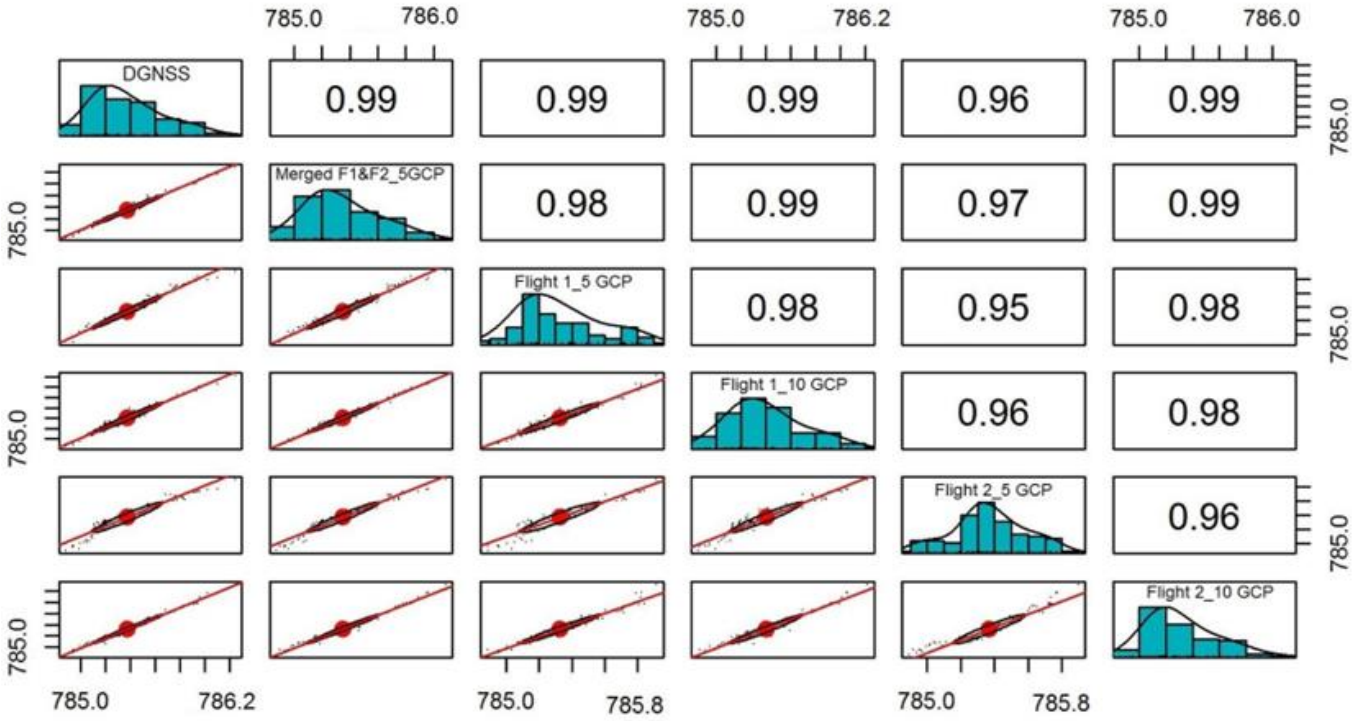

Figure 22. Correlation matrix plot with bivariate scatter plots, distributions, and correlation ellipses of DGNSS non-vegetated elevations and UAS-SfM DSM elevations derived from the combined process of 170 m (Flight 1) and 100 m (Flight 2) AGL nadir images, processed with 5 GCPs using PhotoScan.

3.1.4. Influence of GCP distribution on vertical accuracy

Images of both flights were georeferenced using 5 and 10 GCPs in PhotoScan. The location of 5 GCPs was intentionally selected in the middle of the study area to leave some areas outside of the GCP polygon to analyze the relationship between errors and their distance to the nearest GCP. In Figures 23a and 23b (georeferenced using 5 GCP scheme), the farthest point from the nearest GCP is 267 m; it shows that error increases with distance from GCP. Polynomial regression of 100 samples of difference between SfM DSM elevations and DGNSS in non-vegetated terrain highlights the influence of GCP distribution on vertical error. The figure illustrates that up to a distance of 170 m, almost all of the errors are under 20 cm. As the distance increases, the error also increases gradually, where after 170 m, a 100 m increase in the distance indicates about 1 dm increase in error (in both 100 and 170 m AGL).

For an in-depth investigation of the relationship, images of both flights were georeferenced using 10 GCPs and distributed in a way that most of the validation points fall within the GCP polygon, and the maximum distance of validation points from the GCP cluster is 125 m. Figure 23c and Figure 23d indicate that using 10 GCPs, the correlation between the distance to GCP and the error is weakened, where up to a distance of 100 m, the majority of errors are below 15 cm, most of which range from 0 to 10 cm.

From Figure 23, we conclude that up to 100 m, the correlation between distance to the nearest GCP and vertical error is almost zero in both flights, and positive correlation starts from 100 m, where after 150 m, the vertical error increases dramatically. The results of Pix4Dmapper showed the same trend, which distances greater than 150 m greatly affected the vertical accuracy.

Images of 170 m AGL were processed using the three software without using GCP to evaluate the relative accuracy. The images were aligned and georeferenced using the EXIF geotags. As shown in Table 8, when the images processed without using GCPs, the vertical error ranged from decimeters to meters, which shows the importance of GCPs on accuracy. Figure 24 illustrates the correlation scatter plot matrix of DGNSS elevations and SfM elevation processed without using GCPs.

As the diagram shows, it is not possible to get a strong correlation between the SfM elevation and the DGNSS elevation without GCP because the UAS internal GPS in non-RTK mode cannot yield vertical accuracy comparable with the DGNSS. Nevertheless, the matrix shows a strong elevation correlation between PhotoScan and Pix4D DSMs. 3Dsurvey also shows a positive correlation with both PhotoScan and Pix4D, but the correlation is weak. However, 3D survey produced DSM with less error compared to the other two software (Table 8). Considering the relative accuracy, if the images are scaled with simple measurements instead of georeferencing with GCPs, the DSMs produced using these software packages can be used for many applications such as visualization or in emergency response. However, for obtaining high-accuracy 3D models, georeferencing using GCPs is inevitable.

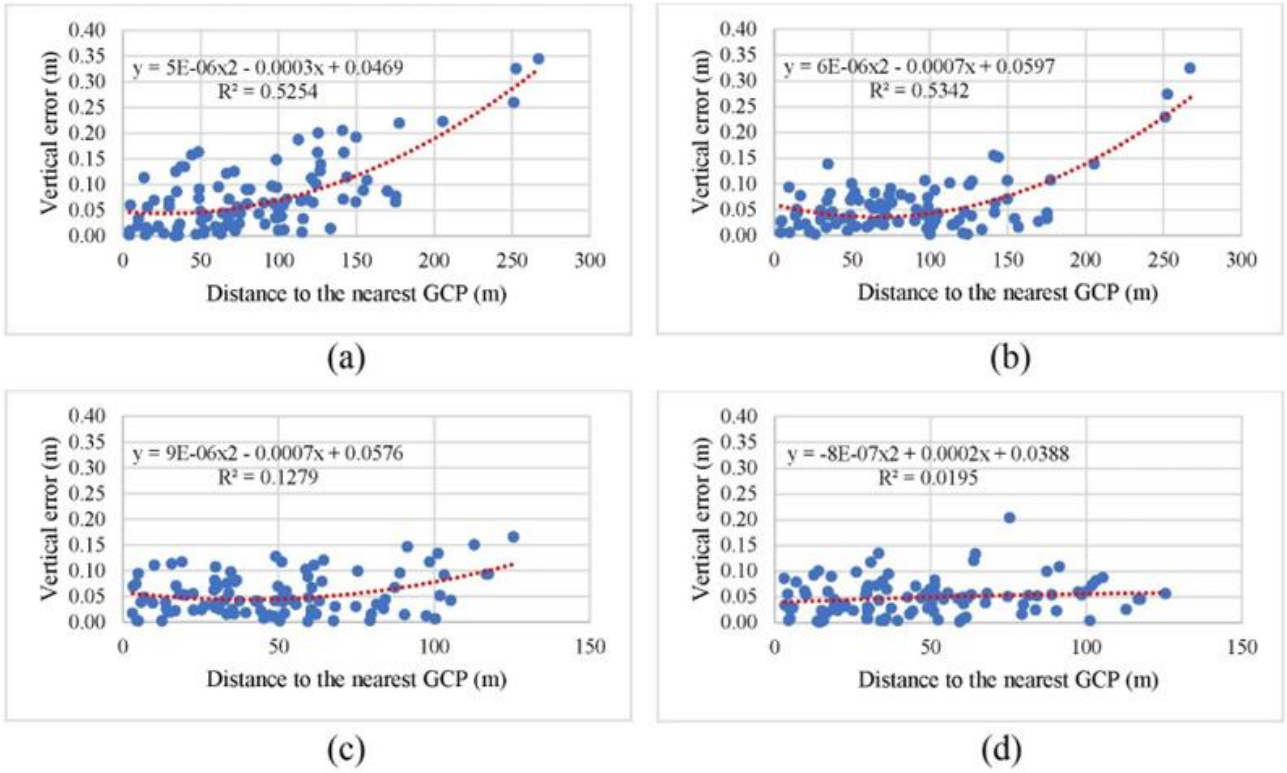

Figure 23. Scatter plot of correlation between distance to the nearest GCP and vertical error. (a) derived from DSM of 100 m AGL nadir images georeferenced with 5 GCPs; (b) derived from DSM of 170 m AGL nadir images georeferenced with 5 GCPs; (c) derived from DSM of 100 m AGL nadir images georeferenced with 10 GCPs (d) derived from DSM of 170 m AGL nadir images georeferenced with 10 GCPs.

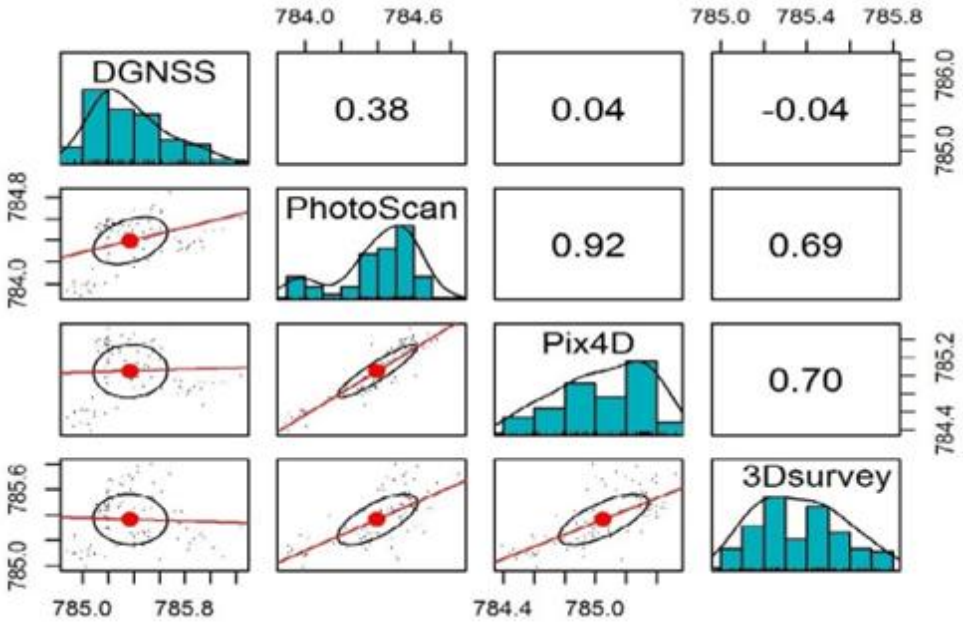

Figure 24. Correlation scatter plot matrix of DGNSS non-vegetated elevations and UAS-SfM DSM elevations derived from 170 m AGL nadir images, processed using the three software without GCP.

4. Conclusion

The aim of this study was to evaluate the accuracy of UAS photogrammetry and structure from motion as a low-cost alternative to terrestrial surveys for geomatics engineering applications. The absolute accuracy assessment showed that the best horizontal and vertical accuracy achieved form the images of 100 m AGL, in which the horizontal RMSE for the orthomosaic was 3 cm, and the vertical RMSE for the DSM was 4 cm. Similarly, orthomosaic with 3 cm horizontal accuracy and DSM with 6 cm vertical accuracy were obtained from the images of 170 m AGL. According to the ASPRS positional accuracy standards for digital geospatial data,

the achieved horizontal accuracies of orthomosaics derived from 100 m and 170 m AGL images meet the ASPRS 2014 horizontal accuracy classes RMSE 2.5 and RMSE 5.0 cm, respectively. These accuracies are equivalent to map scales of 1:100 and 1:200 of ASPRS 1990. In the same way, the obtained vertical accuracies of DSMs derived from 100 and 170 m AGL images in non-vegetated areas are in accordance with Class 3 (RMSE 5 cm) and Class 4 (RMSE 10 cm) of the ASPRS 2014 absolute accuracy, respectively. The equivalent Class 1 contour interval as per ASPRS 1990 is 15 and 30 cm, respectively. The achieved results meet the ASPRS 2014 95% confidence level vertical accuracy of 9.8 and 19 cm, respectively. The analysis results confirm that orthomosaics and DSMs reconstructed from 100 m AGL images can be used for most terrain analysis applications, including civil engineering projects.

This study's findings showed that horizontal accuracy was not affected by flight height; however, flight height greatly affected the vertical accuracy, where a 70 m increase in flight height caused a 3 cm decrease in vertical accuracy. This demonstrated the strong influence of flight height on vertical accuracy. Vertical accuracy was significantly improved by increasing the number of GCPs. The number and distribution of GCPs are crucial in horizontal and vertical accuracy. The vertical accuracy of the DSM processed without GCP is not reliable because the results which were processed without GCPs showed vertical discrepancies in decimeters. Moreover, the results showed that combining two photogrammetric blocks of cross flight images significantly contributes to vertical accuracy and the production of a denser point cloud. The study highlighted that by integrating the images of two different flight heights, outlier values were substantially reduced, and errors showed a normal distribution. Both PhotoScan and Pix4Dmapper generated satisfactory models; however, PhotoScan produced more accurate and high-quality 3D models from images with higher overlap.

Acknowledgement

This paper was extracted from an MSc thesis entitled “Accuracy Analysis and Evaluation of UAS Photogrammetry and Structure from Motion in Engineering Surveying,” conducted by Sayed Ishaq Deliry [77] at Eskisehir Technical University under the supervision of Professor Dr. Uğur Avdan.

Author contributions

Sayed Ishaq Deliry: Conceptualization, Methodology, Data Collection, Analysis, Investigation, Writing - Original Draft, Writing - Review & Editing
Uğur Avdan: Supervision, Validation, Writing - Review & Editing

Conflicts of interest

The authors declare no conflicts of interest.

References

1. Li, Z., Zhu, C., & Gold, C. (2004). Digital terrain modeling: principles and methodology. CRC press.
2. Martínez-Carricondo, P., Agüera-Vega, F., Carvajal-Ramírez, F., Mesas-Carrascosa, F. J., García-Ferrer, A., & Pérez-Porras, F. J. (2018). Assessment of UAV-photogrammetric mapping accuracy based on variation of ground control points. International Journal of Applied Earth Observation and Geoinformation, 72, 1-10. https://doi.org/10.1016/j.jag.2018.05.015
3. Agueera-Vega, F., Carvajal-Ramirez, F., Martínez-Carricondo, P., López, J. S. H., Mesas-Carrascosa, F. J., García-Ferrer, A., & Pérez-Porras, F. J. (2018). Reconstruction of extreme topography from UAV structure from motion photogrammetry. Measurement, 121, 127-138. https://doi.org/10.1016/j.measurement.2018.02.062
4. Ajayi, O. G., Salubi, A. A., Angbas, A. F., & Odigure, M. G. (2017). Generation of accurate digital elevation models from UAV acquired low percentage overlapping images. International Journal of Remote Sensing, 38(8-10), 3113-3134. https://doi.org/10.1080/01431161.2017.1285085
5. Carrivick, J. L., Smith, M. W., & Quincey, D. J. (2016). Structure from motion in the geosciences. John Wiley & Sons.
6. Greenwood, W. W., Lynch, J. P., & Zekkos, D. (2019). Applications of UAVs in civil infrastructure. Journal of Infrastructure Systems, 25(2), 04019002. https://doi.org/10.1061/(ASCE)IS.1943-555X.0000464
7. Nex, F., & Remondino, F. (2014). UAV for 3D mapping applications: a review. Applied Geomatics, 6, 1-15. https://doi.org/10.1007/s12518-013-0120-x
8. International Civil Aviation Organization (2011). Unmanned Aircraft Systems (UAS).
9. Liu, P., Chen, A. Y., Huang, Y. N., Han, J. Y., Lai, J. S., Kang, S. C., ... & Tsai, M. H. (2014). A review of rotorcraft unmanned aerial vehicle (UAV) developments and applications in civil engineering. Smart Structures and Systems, 13(6), 1065-1094. http://dx.doi.org/10.12989/sss.2014.13.6.1065
10. Pajares, G. (2015). Overview and current status of remote sensing applications based on unmanned aerial vehicles (UAVs). Photogrammetric Engineering & Remote Sensing, 81(4), 281-330. https://doi.org/10.14358/PERS.81.4.281
11. Agüera-Vega, F., Carvajal-Ramírez, F., & Martínez-Carricondo, P. (2017). Accuracy of digital surface models and orthophotos derived from unmanned aerial vehicle photogrammetry. Journal of Surveying Engineering, 143(2), 04016025. https://doi.org/10.1061/(ASCE)SU.1943-5428.0000206
12. Awange, J. L. (2012). Environmental monitoring using GNSS: Global navigation satellite systems. Berlin: Springer. https://doi.org/10.1007/978-3-211-73017-1
13. Dai, F., & Lu, M. (2010). Assessing the accuracy of applying photogrammetry to take geometric

measurements on building products. Journal of Construction Engineering and Management, 136(2), 242-250. https://doi.org/10.1061/(ASCE)CO.1943-7862.0000114

14. Ehrhart, M., & Lienhart, W. (2017). Accurate measurements with image-assisted total stations and their prerequisites. Journal of Surveying Engineering, 143(2), 04016024. https://doi.org/10.1061/(ASCE)SU.1943-5428.0000208
15. Holland, D. A., Boyd, D. S., & Marshall, P. (2006). Updating topographic mapping in Great Britain using imagery from high-resolution satellite sensors. ISPRS Journal of Photogrammetry and Remote Sensing, 60(3), 212-223. https://doi.org/10.1016/j.isprsjprs.2006.02.002
16. Honkavaara, E., Arbiol, R., Markelin, L., Martinez, L., Cramer, M., Bovet, S., ... & Veje, N. (2009). Digital airborne photogrammetry—A new tool for quantitative remote sensing?—A state-of-the-art review on radiometric aspects of digital photogrammetric images. Remote Sensing, 1(3), 577-605. https://doi.org/10.3390/rs1030577
17. Kizil, U., & Tisor, L. (2011). Evaluation of RTK-GPS and total station for applications in land surveying. Journal of Earth System Science, 120, 215-221. https://doi.org/10.1007/s12040-011-0044-y
18. Patino, J. E., & Duque, J. C. (2013). A review of regional science applications of satellite remote sensing in urban settings. Computers, Environment and Urban Systems, 37, 1-17. https://doi.org/10.1016/j.compenvurbsys.2012.06.003
19. Slattery, K. T., & Slattery, D. K. (2013). Modeling earth surfaces for highway earthwork computation using terrestrial laser scanning. International Journal of Construction Education and Research, 9(2), 132-146. https://doi.org/10.1080/15578771.2012.700298
20. Telling, J., Lyda, A., Hartzell, P., & Glennie, C. (2017). Review of Earth science research using terrestrial laser scanning. Earth-Science Reviews, 169, 35-68. https://doi.org/10.1016/j.earscirev.2017.04.007
21. Wolf, P. R. (2002). Surveying and mapping: History, current status, and future projections. Journal of Surveying Engineering, 128(3), 79-107. https://doi.org/10.1061/(ASCE)0733-9453(2002)128:3(79)
22. ASCE. (2018). Policy Statement 333 - Engineering surveying definition. https://www.asce.org/advocacy/policy-statements/ps333---engineering-surveying-definition
23. Kreisle, W. E. (1988). History of engineering surveying. Journal of Surveying Engineering, 114(3), 102-124. https://doi.org/10.1061/(ASCE)0733-9453(1988)114:3(102)
24. Bangen, S. G., Wheaton, J. M., Bouwes, N., Bouwes, B., & Jordan, C. (2014). A methodological intercomparison of topographic survey techniques for characterizing wadeable streams and rivers. Geomorphology, 206, 343-361. https://doi.org/10.1016/j.geomorph.2013.10.010
25. Mancini, F., Dubbini, M., Gattelli, M., Stecchi, F., Fabbri, S., & Gabbianelli, G. (2013). Using unmanned aerial vehicles (UAV) for high-resolution reconstruction of topography: The structure from motion approach on coastal environments. Remote Sensing, 5(12), 6880-6898. https://doi.org/10.3390/rs5126880
26. Michelleti, N., Chandler, J. H., & Lane, S. N. (2015). Structure from motion (SFM) photogrammetry. Geomorphological Techniques, 1-12.
27. Deliry, S. I., & Avdan, U. (2021). Accuracy of unmanned aerial systems photogrammetry and structure from motion in surveying and mapping: a review. Journal of the Indian Society of Remote Sensing, 49(8), 1997-2017. https://doi.org/10.1007/s12524-021-01366-x
28. Ullman, S. (1979). The interpretation of visual motion. Massachusetts Inst of Technology Pr.
29. Furukawa, Y., & Ponce, J. (2009). Accurate, dense, and robust multiview stereopsis. IEEE Transactions on Pattern Analysis and Machine Intelligence, 32(8), 1362-1376. https://doi.org/10.1109/TPAMI.2009.161
30. Lowe, D. G. (1999). Object recognition from local scale-invariant features. Proceedings of the Seventh IEEE International Conference on Computer Vision, 2, 1150-1157. https://doi.org/10.1109/ICCV.1999.790410
31. Lowe, D. G. (2004). Distinctive image features from scale-invariant keypoints. International Journal of Computer Vision, 60, 91-110. https://doi.org/10.1023/B:VISI.0000029664.99615.94
32. Snavely, N., Seitz, S. M., & Szeliski, R. (2006). Photo tourism: exploring photo collections in 3D. ACM siggraph 2006 papers, 835-846. https://doi.org/10.1145/1179352.1141964
33. Snavely, N., Seitz, S. M., & Szeliski, R. (2008). Modeling the world from internet photo collections. International Journal of Computer Vision, 80, 189-210. https://doi.org/10.1007/s11263-007-0107-3
34. DeWitt, B. A., & Wolf, P. R. (2000). Elements of Photogrammetry (with Applications in GIS). McGraw-Hill Higher Education.
35. Mölg, N., & Bolch, T. (2017). Structure-from-motion using historical aerial images to analyse changes in glacier surface elevation. Remote Sensing, 9(10), 1021. https://doi.org/10.3390/rs9101021
36. Alptekin, A., & Yakar, M. (2020). Determination of pond volume with using an unmanned aerial vehicle. Mersin Photogrammetry Journal, 2(2), 59-63.
37. Çelik, M. Ö., Alptekin, A., Ünel, F. B., Kuşak, L., & Kanun, E. (2020). The effect of different flight heights on generated digital products: DSM and Orthophoto. Mersin Photogrammetry Journal, 2(1), 1-9.
38. Coveney, S., & Roberts, K. (2017). Lightweight UAV digital elevation models and orthoimagery for environmental applications: data accuracy evaluation and potential for river flood risk modelling. International Journal of Remote Sensing, 38(8-10), 3159-3180. https://doi.org/10.1080/01431161.2017.1292074

39. Deliry, S. I., & Avdan, U. (2023). Accuracy evaluation of UAS photogrammetry and structure from motion in 3D modeling and volumetric calculations. Journal of Applied Remote Sensing, 17(2), 024515. https://doi.org/10.1117/1.JRS.17.024515
40. Fernández, T., Pérez, J. L., Cardenal, J., Gómez, J. M., Colomo, C., & Delgado, J. (2016). Analysis of landslide evolution affecting olive groves using UAV and photogrammetric techniques. Remote Sensing, 8(10), 837. https://doi.org/10.3390/rs8100837
41. Lucieer, A., Jong, S. M. D., & Turner, D. (2014). Mapping landslide displacements using Structure from Motion (SfM) and image correlation of multi-temporal UAV photography. Progress in Physical Geography, 38(1), 97-116. https://doi.org/10.1177/0309133313515293
42. Mesas-Carrascosa, F. J., Notario García, M. D., Meroño de Larriva, J. E., & García-Ferrer, A. (2016). An analysis of the influence of flight parameters in the generation of unmanned aerial vehicle (UAV) orthomosaicks to survey archaeological areas. Sensors, 16(11), 1838. https://doi.org/10.3390/s16111838
43. Öztürk, O., Bilgilioğlu, B. B., Çelik, M. F., Bilgilioğlu, S. S., & Uluğ, R. (2017). İnsanız hava aracı (İHA) görüntüleri ile ortofoto üretiminde yükseklik ve kamera açısının doğruluğa etkisinin araştırılması. Geomatik, 2(3), 135-142. https://doi.org/10.29128/geomatik.327049
44. Sanz-Ablanedo, E., Chandler, J. H., Rodríguez-Pérez, J. R., & Ordóñez, C. (2018). Accuracy of unmanned aerial vehicle (UAV) and SfM photogrammetry survey as a function of the number and location of ground control points used. Remote Sensing, 10(10), 1606. https://doi.org/10.3390/rs10101606
45. Kanun, E., Alptekin, A., Karataş, L., & Yakar, M. (2022). The use of UAV photogrammetry in modeling ancient structures: A case study of "Kanytellis". Advanced UAV, 2(2), 41-50.
46. Colomina, I., & Molina, P. (2014). Unmanned aerial systems for photogrammetry and remote sensing: A review. ISPRS Journal of Photogrammetry and Remote Sensing, 92, 79-97. https://doi.org/10.1016/j.isprsjprs.2014.02.013
47. Goncalves, J. A., & Henriques, R. (2015). UAV photogrammetry for topographic monitoring of coastal areas. ISPRS Journal of Photogrammetry and Remote Sensing, 104, 101-111. https://doi.org/10.1016/j.isprsjprs.2015.02.009
48. Stöcker, C., Bennett, R., Nex, F., Gerke, M., & Zevenbergen, J. (2017). Review of the current state of UAV regulations. Remote Sensing, 9(5), 459. https://doi.org/10.3390/rs9050459
49. Ruzgienė, B., Berteška, T., Gečyte, S., Jakubauskienė, E., & Aksamitauskas, V. Č. (2015). The surface modelling based on UAV Photogrammetry and qualitative estimation. Measurement, 73, 619-627. https://doi.org/10.1016/j.measurement.2015.04.018
50. Long, N., Millescamps, B., Pouget, F., Dumon, A., Lachaussee, N., & Bertin, X. (2016). Accuracy assessment of coastal topography derived from UAV images. In Xxiii Isprs Congress, Commission I, 41, B1, 1127-1134. https://doi.org/10.5194/isprsarchives-XLI-B1-1127-2016
51. Gerke, M., & Przybilla, H. J. (2016). Accuracy analysis of photogrammetric UAV image blocks: Influence of onboard RTK-GNSS and cross flight patterns. Photogrammetrie, Fernerkundung, Geoinformation, 2016(1), 17-30. https://doi.org/10.1127/pfg/2016/0284
52. Tonkin, T. N., & Midgley, N. G. (2016). Ground-control networks for image based surface reconstruction: An investigation of optimum survey designs using UAV derived imagery and structure-from-motion photogrammetry. Remote Sensing, 8(9), 786. https://doi.org/10.3390/rs8090786
53. Oniga, V. E., Breaban, A. I., & Statescu, F. (2018). Determining the optimum number of ground control points for obtaining high precision results based on UAS images. Proceedings, 2(7), 352. https://doi.org/10.3390/ecrs-2-05165
54. American Society for Photogrammetry and Remote Sensing. (2014). ASPRS positional accuracy standards for digital geospatial data. https://doi.org/10.14358/PERS.81.3.A1-A26
55. Reshetyuk, Y., & Mårtensson, S. G. (2016). Generation of highly accurate digital elevation models with unmanned aerial vehicles. The Photogrammetric Record, 31(154), 143-165. https://doi.org/10.1111/phor.12143
56. Agisoft, L. L. C. (2018). Agisoft PhotoScan User Manual: Professional Edition, Version 1.4. Petersburg, Russia: Agisoft LLC.
57. Pix4D, S. A. (2017). Pix4Dmapper 4.1 user manual. Pix4D SA: Lausanne, Switzerland.
58. 3Dsurvey. (2018). 3Dsurvey User Manual: Version 2.7.
59. Jaud, M., Passot, S., Le Bivic, R., Delacourt, C., Grandjean, P., & Le Dantec, N. (2016). Assessing the accuracy of high resolution digital surface models computed by PhotoScan® and MicMac® in sub-optimal survey conditions. Remote Sensing, 8(6), 465. https://doi.org/10.3390/rs8060465
60. Avanzi, F., Bianchi, A., Cina, A., De Michele, C., Maschio, P., Pagliari, D., ... & Rossi, L. (2018). Centimetric accuracy in snow depth using unmanned aerial system photogrammetry and a multistation. Remote Sensing, 10(5), 765. https://doi.org/10.3390/rs10050765
61. Duran, Z., & Atik, M. E. (2021). Accuracy comparison of interior orientation parameters from different photogrammetric software and direct linear transformation method. International Journal of Engineering and Geosciences, 6(2), 74-80. https://doi.org/10.26833/ijeg.691696
62. Gindraux, S., Boesch, R., & Farinotti, D. (2017). Accuracy assessment of digital surface models from unmanned aerial vehicles' imagery on glaciers. Remote Sensing, 9(2), 186. https://doi.org/10.3390/rs9020186
63. Maraş, E. E., & Nasery, N. (2023). Investigating the length, area and volume measurement accuracy of UAV-Based oblique photogrammetry models

produced with and without ground control points. International Journal of Engineering and Geosciences, 8(1), 32-51. https://doi.org/10.26833/ijeg.1017176
64. Nesbit, P. R., & Hugenholtz, C. H. (2019). Enhancing UAV–SFM 3D model accuracy in high-relief landscapes by incorporating oblique images. Remote Sensing, 11(3), 239. https://doi.org/10.3390/rs11030239
65. Ruiz, J. J., Diaz-Mas, L., Perez, F., & Viguria, A. (2013). Evaluating the accuracy of DEM generation algorithms from UAV imagery. The International Archives of the Photogrammetry, Remote Sensing and Spatial Information Sciences, 40, 333-337. https://doi.org/10.5194/isprsarchives-XL-1-W2-333-2013
66. Senkal, E., Kaplan, G., & Avdan, U. (2021). Accuracy assessment of digital surface models from unmanned aerial vehicles' imagery on archaeological sites. International Journal of Engineering and Geosciences, 6(2), 81-89. https://doi.org/10.26833/ijeg.696001
67. American Society for Photogrammetry and Remote Sensing. (1990). ASPRS accuracy standards for large-scale maps, 1068–1070.
68. Benassi, F., Dall'Asta, E., Diotri, F., Forlani, G., Morra di Cella, U., Roncella, R., & Santise, M. (2017). Testing accuracy and repeatability of UAV blocks oriented with GNSS-supported aerial triangulation. Remote Sensing, 9(2), 172. https://doi.org/10.3390/rs9020172
69. Cryderman, C., Mah, S. B., & Shufletoski, A. (2014). Evaluation of UAV photogrammetric accuracy for mapping and earthworks computations. Geomatica, 68(4), 309-317. https://doi.org/10.5623/cig2014-405
70. Rehak, M., & Skaloud, J. (2015). Fixed-wing micro aerial vehicle for accurate corridor mapping. ISPRS Annals of the Photogrammetry, Remote Sensing and Spatial Information Sciences, 2, 23-31. https://doi.org/10.5194/isprsannals-II-1-W1-23-2015
71. Whitehead, K., & Hugenholtz, C. H. (2015). Applying ASPRS accuracy standards to surveys from small unmanned aircraft systems (UAS). Photogrammetric Engineering & Remote Sensing, 81(10), 787-793. https://doi.org/10.14358/PERS.81.10.787
72. Wierzbicki, D., Kedzierski, M., & Fryskowska, A. (2015). Assesment of the influence of UAV image quality on the orthophoto production. The International Archives of the Photogrammetry, Remote Sensing and Spatial Information Sciences, 40, 1-8. https://doi.org/10.5194/isprsarchives-XL-1-W4-1-2015
73. Pérez, M., Agüera, F., & Carvajal, F. (2013). Low cost surveying using an unmanned aerial vehicle. The International Archives of the Photogrammetry, Remote Sensing and Spatial Information Sciences, 40, 311-315. https://doi.org/10.5194/isprsarchives-XL-1-W2-311-2013
74. Hill, A. C. (2019). Economical drone mapping for archaeology: Comparisons of efficiency and accuracy. Journal of Archaeological Science: Reports, 24, 80-91. https://doi.org/10.1016/j.jasrep.2018.12.011
75. Hastaoğlu, K. Ö., Gül, Y., Poyraz, F., & Kara, B. C. (2019). Monitoring 3D areal displacements by a new methodology and software using UAV photogrammetry. International Journal of Applied Earth Observation and Geoinformation, 83, 101916. https://doi.org/10.1016/j.jag.2019.101916
76. Hastaoglu, K. O., Kapicioglu, H. S., Gül, Y., & Poyraz, F. (2023). Investigation of the effect of height difference and geometry of GCP on position accuracy of point cloud in UAV photogrammetry. Survey Review, 55(391), 325-337. https://doi.org/10.1080/00396265.2022.2097998
77. Deliry, S. I. (2020). Accuracy analysis and evaluation of UAS photogrammetry and structure from motion in engineering surveying. [Master's thesis, Anadolu University].